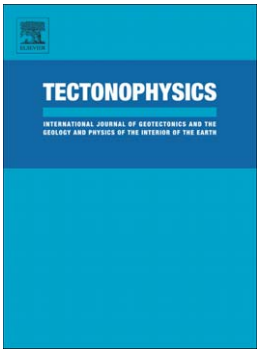

Stability of faults with heterogeneous friction properties and effective normal stress

Yingdi Luo, Jean-Paul Ampuero

PII: S0040-1951(17)30459-6
DOI: doi:10.1016/j.tecto.2017.11.006
Reference: TECTO 127672

To appear in: *Tectonophysics*

Received date: 16 August 2017
Revised date: 15 October 2017
Accepted date: 4 November 2017

Please cite this article as: Luo, Yingdi, Ampuero, Jean-Paul, Stability of faults with heterogeneous friction properties and effective normal stress, *Tectonophysics* (2017), doi:10.1016/j.tecto.2017.11.006

Stability of faults with heterogeneous friction properties and effective normal stress

Yingdi Luo (luoyd@gps.caltech.edu)[1] and Jean-Paul Ampuero[1]

[1]Seismological Laboratory, California Institute of Technology, CA 91125, USA

Abstract

Abundant geological, seismological and experimental evidence of the heterogeneous structure of natural faults motivates the theoretical and computational study of the mechanical behavior of heterogeneous frictional interfaces. Fault zones are composed of a mixture of materials with contrasting strength, which may affect the spatial variability of seismic coupling, the location of high-frequency radiation and the diversity of slip behavior observed in natural faults. To develop a quantitative understanding of the effect of strength heterogeneity on the mechanical behavior of faults, here we investigate a fault model with spatially variable frictional properties and pore pressure. Conceptually, this model may correspond to two rough surfaces in contact along discrete asperities, the space in between being filled by compressed gouge. The asperities have different permeability than the gouge matrix and may be hydraulically sealed, resulting in different pore pressure. We consider faults governed by rate-and-state friction, with mixtures of velocity-weakening and velocity-strengthening materials and contrasts of effective normal stress. We systematically study the diversity of slip behaviors generated by this model through multi-cycle simulations and linear stability analysis. The fault can be either stable without spontaneous slip transients, or unstable with spontaneous rupture. When the fault is unstable, slip can rupture either part or the entire fault. In some cases the fault alternates between these behaviors throughout multiple cycles. We determine how the fault behavior is controlled by the proportion of velocity-weakening and velocity-strengthening materials, their relative strength and other frictional properties. We also develop, through heuristic approximations, closed-form equations to predict the stability of slip on heterogeneous faults. Our study shows that a fault model with heterogeneous materials and pore pressure contrasts is a viable framework to reproduce the full spectrum of fault behaviors observed in natural faults: from fast earthquakes, to slow transients, to stable sliding. In particular, this model constitutes a building block for models of episodic tremor and slow slip events.

Keywords: fault heterogeneity; heterogeneous pore-pressure; slip instability; earthquakes; rate-and-state friction; linear stability analysis

Highlights:

1. A comprehensive study of slip behaviors in fault models with mixed velocity-strengthening / velocity-weakening materials and heterogeneous effective normal stress
2. Fault stability investigated with numerical rate-and-state simulations and analytical linear stability analysis
3. Rich range of slip behaviors including steady-slip, slow aseismic slip transients, ruptures localized in part of the fault (P-instability), ruptures breaking the whole fault (T-instability) and combinations of both
4. Closed form equations that accurately describe the stability conditions for P-instabilities and T-instabilities
5. A useful framework to understand the full spectrum of slow-to-fast earthquakes

1 Introduction

1.1 Geological and physical background

The spectrum of earthquake phenomena has been greatly expanded by the discovery in the past decade of a variety of slow earthquake processes including low frequency earthquakes (LFE), tectonic tremors (also known as non-volcanic tremors, NVT), very low frequency earthquakes (VLFE) and slow-slip events (SSE) (Ide et al. 2007). These seismic and aseismic events often occur together (Gomberg 2010). For instance, recurrent SSE are often accompanied by tremors, a phenomenon known in Cascadia as "episodic tremor and slip" (ETS) (Rogers and Dragert 2003). These slow earthquake phenomena mostly occur in the deep seismic-aseismic transition region of faults, or in the shallow accretionary prism of subduction zones. For instance, in the Cascadia subduction zone ETS are located below the seismogenic depth limit determined by thermal modeling (Hyndman and Wang 1993; Peacock 2009). In most cases, the transition from fast to slow, to steady slip behavior as a function of depth is gradual: e.g. Wech and Creager (2011) showed that with increasing depth, the inter-event time between episodic slow events (ETS and episodic tremors) and their duration decrease gradually. The amount of background (non-episodic, continuous) tremors increases with depth, and eventually the fault transitions into steady slip.

Regular earthquakes (i.e. earthquakes with rupture speed comparable to wave speeds) may also feature intermingled slow and fast rupture processes. Teleseismic back-projection source imaging of the 2011 Tohoku-Oki earthquake revealed a period of relatively slow rupture in the down-dip direction (Meng et al. 2011). Counterintuitively, this slow stage of the rupture was interspersed by strong high-frequency radiation bursts, indicating patches of fast slip. The frequency content of this deeper part of the rupture, near the bottom of the seismogenic zone, was richer in high frequencies than the shallower part. This depth-dependent frequency content of the source has been observed in other megathrusts events, including the 2015 Gorkha, Nepal earthquake (Avouac et al. 2015; Lay et al. 2012). Seismological and geodetic observations of non uniform seismic coupling, non uniform earthquake slip, and slow slip and tremor have indeed promoted the view that subduction earthquake processes are significantly affected by the heterogeneity of fault zone mechanical properties, often represented conceptually as fault asperities (Dragert 2007; Ito et al. 2007; Lay and Kanamori 1981; Seno 2003).

These gradual transitions and coexistence of fast and slow earthquake slip behaviors in different environments suggest common mechanisms behind the full spectrum of earthquakes. Various studies have been conducted to study specific aspects of fast and slow slip transients (e.g. Ando et al. 2010; Leeman et al. 2016; Mclaskey and Yamashita 2017; Nakata et al. 2011). Yet there is currently no model that can conceptually unify and quantitatively reproduce such a large span of phenomena. This gap in our understanding of the mechanics of fast and slow earthquakes has encouraged us to search for viable physical models, and the present work is a building block in that effort.

Geological field observations show heterogeneity of fault materials over a broad range of length scales. Exhumed subduction fault zones show a pattern of block-in-matrix mélange, with competent lenses embedded in an incompetent matrix, at scales ranging from millimeters to tens of meters (Bebout and Barton 2002; Fagereng 2011; Fagereng and Cooper 2010; Fagereng and Sibson 2010; Meneghini et al. 2010). Laboratory experiments indicate that heterogeneity can affect the mechanical response of a fault. Kocharyan et al. (2016) found in laboratory experiments that the stress drop of slip transients depends on the proportion of materials mixed in a composite gouge. Ma and He (2001) found period doubling phenomena in experiments with two different materials along a frictional surface. Thus, fault heterogeneity involving contrasts of material strength is a potentially important ingredient to model rich fault slip behaviors.

Geological observations also show evidence of spatial and temporal variability of pore fluid pressure across various scales in fault zones. This contributes to fault heterogeneity and can affect fault slip behavior. Mechanisms such as hydraulic fracturing and cracking (Luo and Vasseur 2002), and pore-space reduction by solution and cementation (Rittenhouse 1971) change the permeability of fault materials, affect the pore pressure and hence the frictional strength. The formation of fluid seals in a fault zone causes high pore pressures if the sealed material compacts or produces more fluids. Excess pressure can then be released by rupture of the seals, over the long time scales of plate subduction, or recur with fault-valve behavior over the time periods between earthquakes (Hillers and Miller 2007; Sibson 1992, 2014; Sibson et al. 1988). Also, multiple direct and indirect evidence show localized changes in pore pressure. Healy et al. (1968) and a body of subsequent work studies seismicity changes due to changes of pore pressure. Thermal expansion of pore fluids, e.g. via shear heating, in media with heterogeneous permeability can create highly localized pore pressure contrasts (Osborne and Swarbrick 1997). Roberts and Nunn (1995) found that fluid transport results in localized pore pressure changes on various time scales. Fagereng and den Hartog (2017) studied pressure solution

at seismogenic depths and found that more soluble elements dissolve first, which causes porosity and pore pressure differences between competent and incompetent fault materials at fine length scales of material heterogeneity.

Other fault properties can also be heterogeneous, such as the characteristic slip distance D_c of the evolution of friction (see definition in section 2). Marone and Kilgore (1993) found, in laboratory experiments, a scaling between D_c and the thickness of the gouge layer, a fault zone property that shows significant variability along natural faults. Scuderi and Collettini (2016) found that D_c is positively related to normal stress, which can also be variable along a fault. Parsons (2005) hypothesized that temporal changes of D_c could help explain dynamic triggering. Hillers et al. (2006, 2007) and Perfettini et al. (2003) studied the effect of heterogeneity of D_c on earthquake nucleation and earthquake cycle models. Luo et al. (2017b) also considered a fault with heterogeneous D_c to model earthquakes with a wide range of magnitudes for a study of earthquake scaling relations.

Here, we develop a conceptual model consistent with the foregoing picture of heterogeneous faults. Our modeling framework is generally applicable to faults with variable strength and pore pressure, regardless of how those heterogeneities emerged. However, it may be useful to illustrate the model through one specific situation. Consider a fault zone composed of gouge or sediments sandwiched in between two rough surfaces. When the two fault surfaces are pressed together by the increasing confining stresses during subduction, the rough surfaces make contact at discrete "asperities" and the intervening gouge matrix is compressed. The asperity contacts can have different compressibility and permeability than the gouge matrix and can be prone to hydraulic sealing (Figure 1). Influx of fluids, e.g. due to dehydration, can change the pore pressure in the gouge but not in the sealed asperities. These mechanisms can result in differences of effective normal stress between asperities and the gouge matrix.

1.2 Background on fault stability

In theoretical and computational models, a fault can display a wide range of slip behaviors. We refer to a fault as “stable” if it slips steadily when driven by a steady loading. If instead the fault generates spontaneous slip transients, we qualify it as “unstable”. On unstable faults, slip transients range from quasi-static (aseismic, such as SSE) to dynamic (seismic, such as regular earthquakes). One possible way, proposed here, to distinguish between aseismic and seismic slip transients, is based on radiation efficiency, i.e. the ratio of radiated energy to the sum of radiated and fracture energies. The radiation efficiency of an earthquake or any propagating slip transient is primarily controlled by its rupture speed (Venkataraman and Kanamori 2004). The stability of a fault depends on its frictional properties, state of stress and boundary conditions, as will be explained in detail in section 2 within the framework of rate-and-state friction. Rice and Ben-Zion (1996) summarized studies of earthquake models that gave rise to slip complexities. The propensity to stability of a rate-and-state material depends strongly on whether its steady-state friction coefficient is velocity-weakening (VW) or velocity-strengthening (VS). A VW material can be unstable and will represent here a competent fault zone material, whereas a VS material tends to be stable.

Our study extends previous theoretical and computational work on the stability of faults governed by rate-and-state friction with an alternation of VW and VS materials. Skarbek et al. (2012) studied fault stability as a function of the ratio of VW to VS material content. They found that, with other parameters fixed, the relative portion of the VW and VS materials controls the stability of slip. They focused on instabilities that involve rapid slip over the whole fault, which we will refer to as "Total instabilities" or "T-instabilities". They found the critical VW/VS area ratio required for instability in numerical simulations is accurately predicted by linear stability analysis. Dublanchet et al. (2013) introduced the concept of a critical (minimum) density of VW asperities required for instability. Their results are consistent with those of Skarbek et al. (2012). Yabe and Ide (2017) reported an additional instability that involves rapid slip in the VW segments, possibly with minor slip extending to the VS material in their immediate vicinity. We will refer to these as "Partial instabilities" or "P-instabilities". The existence of P-instabilities is not unexpected: it is known that an isolated VW fault is unstable if its size exceeds a critical length (Chen and Lapusta 2009; Rubin and Ampuero 2005). Yabe and Ide (2017) argued that the P-instability occurs when the size of the VW segment exceeds the critical size for instability on a homogeneous VW fault. We will show in section 2 that such argument, while adequate to first-order, is incomplete: the P-instability is affected by the surrounding VS material as well. They also found that, if the loading stiffness is very low, the T-instability occurs only if the fault is velocity neutral on average (average $a - b = 0$). This condition can be derived as a special case of the theoretical results by Skarbek et al. (2012). Viesca (2016) further studied the evolution of slip rate during the nucleation of frictional instabilities on heterogeneous faults.

1.3 Goals and scope of this study

We focus on the following two questions about faults with strength and pore pressure contrasts, within the framework of rate-and-state faults with alternating VS and VW properties:

1. Under what conditions is the fault stable or unstable?
2. Does unstable slip span the whole fault or only part of it?

In particular, our study includes an investigation on the effect of heterogeneous characteristic slip distance D_c, fault width W, and effective normal stress contrast between the VW and VS materials, which have not been considered in previous studies. Allowing variations of pore pressure and D_c unveils unexpected characteristics of instabilities that are of theoretical and practical significance.

In section 2, we introduce the model and study numerically its stability as a function of the proportion of VW and VS materials, their relative strength and the degree of intrinsic instability of the VW asperity. In section 3, we utilize linear stability analysis (LSA) to study the stability of a simplified two-degree-of-freedom spring-block model. The results are in good agreement with the instability conditions found numerically in section 2. The role of other model parameters is then explored more comprehensively via LSA. In section 4, we develop compact formulas in closed form which accurately predict the instability conditions based on heuristic approximations of the LSA results. Finally, in section 5, we discuss implications of our results and conclude.

2 Rate-and-state models

2.1 Model definition

We adopt the classical rate-and-state friction law motivated by laboratory experiments at low slip rate (Dieterich 1979; Marone 1998; Ruina 1983). This friction law has shown its modeling capacity from laboratory scales to natural earthquake scales (Ampuero and Rubin 2008). The rate-and-state framework assumes that the fault is always slipping and hence the shear stress τ remains equal to the frictional strength, $\tau = \mu\sigma$, where σ is the effective normal stress (normal stress minus pore fluid pressure). The friction coefficient $\mu(V, \theta)$ depends on slip velocity V and on a state variable θ. We adopt the most basic and commonly used form:

$$\mu(V, \theta) = \mu^* + a \ln \frac{V}{V^*} + b \ln \frac{V^* \theta}{D_c} \tag{1}$$

where μ^* is the reference friction coefficient, V^* the reference slip rate, D_c the characteristic slip distance of state evolution, a and b the constitutive parameters quantifying the importance of the direct and evolution effects, respectively. The state variable θ evolves with time, as described by empirical evolution laws. Here we adopt the so-called "slip law", the state evolution law that is most consistent with laboratory experiments (Bhattacharya et al. 2015):

$$\dot{\theta} = -\frac{V\theta}{D_c} \ln \frac{V\theta}{D_c} \tag{2}$$

At steady state, when $\dot{\theta} = 0$, the friction coefficient is

$$\mu_{ss}(V) \doteq \mu(V, D_c/V) = \mu^* + (a - b) \ln \frac{V}{V^*} \tag{3}$$

When $a - b < 0$, the fault is velocity-weakening (VW): the steady-state friction coefficient $\mu_{ss}(V)$ decreases as slip rate increases. Spontaneous slip transients occur if the fault stiffness (which is inversely proportional to the fault size) is below a critical stiffness that depends on friction properties and effective normal stress. A VW fault is conditionally stable: it is unstable if its size L exceeds a certain critical length

$$L_c = \frac{G D_c}{\sigma(b - a)} \tag{4}$$

where G is the shear modulus of the host rock. We refer to a fault with size larger than L_c as *supercritical*. An unstable VW fault is seismic if $L \gg L_c$ (very supercritical) and aseismic if $L \gtrapprox L_c$ (slightly supercritical). If $L < L_c$, we

qualify the fault as subcritical. Under the slip law, a subcritical fault is stable when driven by steady loading, but can develop fast slip transients if stimulated by an external perturbation of sufficiently large amplitude (Gu and Wong 1994). If $a - b > 0$, the fault is velocity-strengthening (VS). A VS fault is stable, but it can host slip transients when perturbed (e.g. Perfettini and Ampuero 2008).

We adopt a minimalistic approach to model the effects of having a mixture of materials in a fault zone. Fault heterogeneity spans a large range of length scales in nature (Fagereng 2011) and in our conceptual model (Figure 1). We consider a simplified representation of heterogeneous faults: we represent the asperity contacts and the gouge matrix as VW and VS materials, respectively (Figure 2 (A)). The spatial distribution of these materials along the fault is then simplified as 1D strips oriented in the along-dip direction (Figure 2 (B)). We further assume the pattern of material heterogeneity repeats in space, with a spatial period L containing one VW strip and one VS strip (Figure 2 (C)). We assume that slip remains spatially periodic, also with spatial period L. In this way, the heterogeneous fault is reduced to an infinitely long, linear fault in a 2D medium with periodic alternation of VW and VS segments (Figure 2 (D)). These simplifications allow us to do the simulations on a single period of the heterogeneous pattern, reducing computational cost significantly and allowing a broad parametric study.

We examine the behavior of the model numerically, by performing multi-cycle quasi-dynamic simulations. The quasi-dynamic approach utilizes radiation damping to approximate the effect of inertia (Rice 1993). We employ the open source software QDYN developed by Luo et al. (2017a), which utilizes the boundary element method (used in rate-and-state earthquake simulations since Tse and Rice (1986)) and adaptive time-stepping. The software QDYN is publicly available at Github (https://github.com/ydluo/qdyn). To focus on features that are independent of the arbitrary initial conditions, we perform multi-cycle simulations and discard the initial "warm-up" cycles from our analysis.

To incorporate the effect of the missing third dimension while keeping the computational efficiency of a 2D model, we adopt a 2.5D approximation similar to that introduced by Hawthorne and Rubin (2013). We consider a 2D fault embedded in an unbounded elastic 3D medium. The fault is infinitely long in the along-strike direction, but has a finite width W along dip. We assume the depth-dependence of slip is known, sinusoidal, and the same at all positions along strike. The overall amplitude of slip is allowed to vary along strike. These assumptions allow us to reduce the 3D problem to a 2.5D problem in which we solve only for slip variations along strike. The static stress transfer involves convolution between slip and an elasto-static stress interaction kernel, which is efficiently computed via Fast-Fourier Transform (FFT). A derivation of the 2.5D static kernel in spectral domain is given in Appendix A.2.

To further simplify the problem, we assume slip is uniform within the VW segment. Thus in practice, the VW segment is represented by a single computational cell, while the VS segment is a continuum in which slip is well resolved in space and time. This assumption is a reasonable compromise: it does not affect significantly the conditions for stability and it reduces substantially the computational cost, allowing us to conduct a comprehensive parametric study. In fact, we will demonstrate that our modeling results, obtained under this simplifying assumption, are consistent with those of previous studies in which non-uniform slip inside the VW segment is considered (Skarbek et al. 2012).

2.2 Non-dimensional model parameters and parametric study program

Table 1 shows the list of symbols adopted here, the corresponding range of parameters studied and the typical values of model parameters. Despite being minimalistic, the model has as many as seven independent non-dimensional numbers:

1. *Relative strength* $\alpha = \frac{(b_w - a_w)\sigma_w}{(a_s - b_s))\sigma_s}$ is the ratio between the amount of weakening in the VW area to the amount of strengthening in the VS area, due to heterogeneity of $|b - a|\sigma$.

2. *Individual criticalness of the VW segment* $\beta = \frac{L_w}{L_{cw}} = \frac{L_w(b_w - a_w)\sigma_w}{GD_{cw}}$ is the ratio between the size of the VW segment, L_w, and the critical nucleation size of the VW material, L_{cw} (defined as in Equation 4). If the VW segment were isolated, instead of embedded in a VS matrix, it would be unstable if $\beta > 1$.

3. *VW/VS area ratio* $f = L_w/L_s$, where L_s is the size of the VS segment.

4. *VW/VS characteristic slip distance ratio* $\xi^2 = D_{cw}/D_{cs}$. It is arbitrarily constrained in our rate-and-state models by the relation $\xi^2 = \frac{f}{1+f}\frac{\alpha}{6\beta}$. This arbitrary constraint is released in section 3.

5. *Fault aspect ratio* $W' = W/L$ is the ratio of the fault width, W, to the spatial period of fault heterogeneity, L.

6. a/b *ratio of the VW segment*, $\gamma_w = a_w/b_w$.

physical properties	value
fault period L	200 m
fault width W	110 km $(primary)$ | 11 km | 1.1 km
shear modulus G (Lamé's second parameter)	30 GPa
shear wave velocity	3000 m/s
reference friction coefficient μ^*	0.6
tectonic loading rate $V_{pl} = V^*$	10^{-9} m/s
VW/VS area ratio f	1 | 1/3 | 1/7
VW effective normal stress σ_w	0.5-250 MPa (various)
VS effective normal stress σ_s	5 MPa
VW characteristic slip distance D_{cw}	$4 \times 10^{-8} - 4 \times 10^{-1}$ m
VS characteristic slip distance D_{cs}	4×10^{-4} m $(primary)$ | 4×10^{-3} m
VW friction coefficient a_w (direct effect)	0.009
VW friction coefficient b_w (indirect effect)	0.01
VS friction coefficient a_s (direct effect)	0.012
VS friction coefficient b_s (indirect effect)	0.01
L_{cs}/L ($L_{cs} = \frac{\mu D_{cs}}{(a_s - b_s)\sigma_s}$)	6

Table 1: Typical values of parameters used in rate-and-state simulation, individual values are held constant in each simulation.

7. *a/b ratio of the VS segment*, $\gamma_s = a_s/b_s$.

Skarbek et al. (2012) studied the effect of f, γ_w and γ_s on the fault stability of a fault model with heterogeneous friction but uniform effective normal stress. In this work, we study the role of the first five non-dimensional numbers listed above. In this section, we focus on the first three non-dimensional numbers. The results will serve as reference in section 3 to validate the LSA approach. Once the agreement between rate-and-state QDYN simulations and LSA is demonstrated, the less computationally demanding LSA will allow us to study the model behavior over a broader range of parameters and to develop more general implications.

The program of the parametric study in this section is summarized as follows. We perform QDYN simulations varying the VW/VS area ratio, f, fault relative strength, α, and criticalness of the VW segment, β, while keeping $a_w, a_s, b_w, b_s, \sigma_s$ and D_{cs} fixed. We vary α by changing σ_w. This also changes β, but we further control β by varying D_{cw}. We consider three different values of $f = 1, 1/3$ and $1/7$. Defining a characteristic length in the VS segment as $L_{cs} = \frac{\mu D_{cs}}{(a_s - b_s)\sigma_s}$, we keep the ratio L_{cs}/L fixed and equal to an arbitrary value of 6. This ratio is related to other non-dimensional numbers by $L_{cs}/L = \frac{f}{1+f}\frac{\alpha}{\beta\xi^2}$. Hence our approach also changes ξ, following the relation $\xi^2 = \frac{f}{1+f}\frac{\alpha}{6\beta}$. Later in section 3, we release this arbitrary constraint and use LSA to explore the effect of L_{cs}/L, characteristic slip distance ratio $\xi^2 = D_{cw}/D_{cs}$ and fault aspect ratio W'.

2.3 Results of numerical simulations

The results of a set of simulations with fixed $f = 1/7$ and varying α and β are summarized in Figure 3 top, which shows the peak slip rate reached in the VW segment as a function of α and β. Results for the case $f = 1$ are shown in Figure 3 bottom. A peak slip rate higher than the tectonic slip rate $V_{pl} = 10^{-9}$ m/s indicates fault instability manifested by spontaneous slip transients. We further quantify the uniformity of slip along the fault in Figure 4 by the maximum of the ratio between the slip rates on the VW segment and at the center of the VS segment (measured at the same time). We find that the fault stability depends on α and β, and displays a rich spectrum of slip behaviors:

1. *Stable slip* (left and lower-left of Figures 3 and 4 in blue). At low β, below a certain minimum value β_{min}, the whole fault is stable for all α. At intermediate $\beta > \beta_{min}$, the fault is stable only for α smaller than a certain value α_T that depends on β.

2. *Total instability* (upper-right of Figures 3 and 4). When $\alpha > \alpha_T(\beta)$, the whole fault is unstable: both the VW and VS segments slip episodically. This is the total instability we coined "T-instability". The value of $\alpha_T(\beta)$

decreases with increasing β, and converges to a constant value α_{Tc}. We observe that $\alpha_{Tc} \approx 1/f$ (Figures 5 and 3). Two main patterns of slip are observed in T-instabilities (Figure 4). When α is slightly above $\alpha_T(\beta)$, unstable slip is uniform along the whole fault (Figure 4; see also slip patterns in Figure 6(A)). With the increase of α, fault slip gradually transits into more complicated patterns. When α is well above $\alpha_T(\beta)$, instability with non-uniform slip occurs, with localized nucleation near the asperity followed by slip propagation over the whole fault. Such distinct behaviors of T-instabilities have been previously identified in laboratory experiments of VW-VS interaction, e.g. quadrants I and III in Figure 1 of (Mclaskey and Yamashita 2017) show T-instabilities of uniform slip and localized nucleation, respectively. In this regime we also observe multi-stage super-cycle behavior in which T-instabilities are preceded by one or multiple failures that start in the VW segment but do not propagate over the whole fault (Figure 6(C)). In super-cycles with multiple precursors, each precursor consistently penetrates further into the VS area and the inter-event time between each precursor shortens until a large event ruptures the whole fault. The inter-event time and magnitude of T-instabilities increase with increasing α and decreasing β (Figure 7). Near the T-instability boundary, there is a narrow transitional regime where the fault slips aseismically (yellow-to-green color in Figure 3)

3. *Partial instability* (lower-right of Figures 3 and 4). At larger β, above a certain $\beta_{P\_min} \approx 1$, and low α, below a certain $\alpha_P(\beta) < \alpha_{Tc}$, partial instabilities occur in which unstable slip is mainly confined to the VW segment (Figures 4 and 6(B)). We refer to these as "P-instabilities". Their existence is expected from the instability of an isolated VW segment, without surrounding VS segments, whose size exceeds the critical nucleation size L_c (Ampuero and Rubin 2008; Rubin and Ampuero 2005). However, such interpretation predicts the P-instability should happen at a critical value of β, independent of α. This would correspond to a vertical stability boundary in Figures 3 and 4, but our simulation results show instead a significantly curved stability boundary. Thus, the interaction between VW and VS parts of the fault influences the P-instability. The inter-event time and magnitude of P-instabilities are much smaller than those of T-instabilities. The ratio of both inter-event time and magnitude between T-instability and P-instability are roughly proportional to the ratio of W/L_w (Figure 7). Also, the inter-event time of P-instabilities, their magnitude and their rupture penetration distance into the VS area, all increase with increasing α (Figure 7). If α increases, P-instabilities eventually merge with T-instabilities. If β is large this transition is direct, but at intermediate values of $\beta \approx 1$ a transitional stable regime exists between P-instability and T-instability (Figures 3 and 4) .

4. At large $\beta > \beta_{max}$ (to the right of Figure 3 and 4) the fault is unstable for any α, by either P-instability or T-instability. At low α, roughly below α_{Tc}, P-instability occurs. At high $\alpha > \alpha_{Tc}$, T-instability occurs with non-uniform slip. We observe no instability with uniform slip in our simulations with $\beta > \beta_{max}$. Slip behavior can be complicated near the zone of convergence of T-instability and P-instability (Figure 6(D)). We see super-cycles interspersed by clustered occurrences of rupture of the VW segment, with short inter-event-times, and penetrating substantially into the VS part.

3 Linear stability analysis

3.1 Model assumptions and analysis concepts

To gain a fundamental understanding of the unstable regimes observed in our QDYN simulations, we perform a theoretical study of a simplified model: a periodic two-degree-of-freedom spring-block system. To simplify the problem while preserving its essence, we assume that slip is uniform within each VW and VS segment. The model is thus reduced to a Burridge-Knopoff model: a linear array of blocks connected by springs and loaded at constant velocity through side springs (Burridge and Knopoff 1967). Exploiting the assumed periodic alternation of VW and VS blocks, the model is further reduced to a two-degree-of-freedom system with periodic boundary conditions (Figure 8).

The stability of a non-linear system can be studied by linear stability analysis (LSA). The analysis evaluates the stability of perturbations with respect to a reference solution. The governing equations are first linearized in the vicinity of the reference solution, and written in the form of $\frac{dx}{dt} = \bar{\bar{A}}x$, where $\bar{\bar{A}}$ is a linear operator. Perturbations are unstable if at least one of the eigenvalues of $\bar{\bar{A}}$ has a positive real part. In that case any small perturbation to the system diverges exponentially away from the reference state. Otherwise, if all the eigenvalues of $\bar{\bar{A}}$ have negative real parts, perturbations are exponentially damped and the system is linearly stable at the reference state (Glendinning

1994). LSA was employed also by Skarbek et al. (2012), but assuming uniform normal stress, non-periodic boundary conditions and loading from the side.

3.2 LSA derivation

With the aforementioned simplifications, we utilize LSA to analyze the stability of the system. The analysis is summarized in three steps.

The first step is the derivation of the governing equations. This is done in Appendix A.1, starting from the discrete stress transfer equations and extending the result to an arbitrary proportion of VW and VS materials. For a periodic two-degree-of-freedom VW-VS system with arbitrary area ratio, we obtain the following governing equation:

$$\tau_w = K_I(V_{pl}t - d_w) + K_{II}(d_s - d_w) \tag{5}$$
$$\tau_s = K_I(V_{pl}t - d_s) + fK_{II}(d_w - d_s) \tag{6}$$

where τ_w and τ_s, d_w and d_s are the shear stresses and slips of the VW and VS segments, respectively; $K_I = K_w = \pi G/W$ is the stiffness of the remote loading; $K_{II} = K_0 - K_w$ is the stiffness corresponding to inter-block interactions; and K_0 is the self-stiffness of the VW block.

The second step is to linearize the governing equations and formulate the eigenvalue problem. This is done in Appendix A.3). We find that the eigenvalues of the linearized operator are the roots λ of

$$\det(Q(\lambda)) = 0 \tag{7}$$

where

$$\begin{aligned} Q(\lambda) = &\begin{pmatrix} a_w\sigma_w/V_{pl} & 0 \\ 0 & a_s\sigma_s/V_{pl} \end{pmatrix}\lambda^2 \\ &+ \begin{pmatrix} (a_w - b_w)\sigma_w/D_{cw} + K_I + K_{II} & -K_{II} \\ -fK_{II} & (a_s - b_s)\sigma_s/D_{cs} + K_I + fK_{II} \end{pmatrix}\lambda \\ &+ \begin{pmatrix} (K_I + K_{II})V_{pl}/D_{cw} & -K_{II}V_{pl}/D_{cw} \\ -fK_{II}V_{pl}/D_{cs} & (K_I + fK_{II})V_{pl}/D_{cs} \end{pmatrix} \end{aligned} \tag{8}$$

The third step is to solve the instability condition and determine the stability boundary. The system is unstable if the real part of at least one eigenvalue is positive. We introduce the following shorthand notations:

$$A_i = a_i\sigma_i \quad \text{and} \quad B_i = b_i\sigma_i \tag{9}$$

Equation 7 is a quartic equation:

$$\det(Q) = s_4\lambda^4 + s_3\lambda^3 + s_2\lambda^2 + s_1\lambda + s_0 = 0 \tag{10}$$

where

$$s_0 = K_I(K_I + (1 + f)K_{II}) \tag{11}$$
$$s_1V_{pl} = K_I(K_I + (1 + f)K_{II})(D_{cw} + D_{cs}) + (A_w - B_w)(K_I + fK_{II}) + (A_s - B_s)(K_I + K_{II}) \tag{12}$$
$$\begin{aligned} s_2V_{pl}^2 = &K_I(K_I + (1 + f)K_{II})D_{cw}D_{cs} + (A_w - B_w)(A_s - B_s) \\ &+ (A_wD_{cw} + (A_w - B_w)D_{cs})(K_I + fK_{II}) + (A_sD_{cs} + (A_s - B_s)D_{cw})(K_I + K_{II}) \end{aligned} \tag{13}$$
$$s_3V_{pl}^3 = A_wA_s(D_{cw} + D_{cs}) - A_wB_sD_{cw} - A_sB_wD_{cs} + A_sD_{cw}D_{cs}(K_I + K_{II}) + A_wD_{cw}D_{cs}(K_I + fK_{II}) \tag{14}$$
$$s_4V_{pl}^4 = A_wA_sD_{cw}D_{cs} \tag{15}$$

We now focus on stability boundaries, across which the real part of λ changes sign. We thus look only for roots with zero real part (purely imaginary). If λ is purely imaginary, the real and imaginary parts of Equation 10 give two equations:

$$s_4\lambda^4 + s_2\lambda^2 + s_0 = 0 \tag{16}$$
$$s_3\lambda^3 + s_1\lambda = 0 \tag{17}$$

Equation 17 gives $\lambda^2 = -s_1/s_3$. Plugging that into Equation 16 gives the condition at instability boundaries:

$$s_1(s_4 s_1 - s_2 s_3) + s_0 s_3^2 = 0 \tag{18}$$

In the particular case of uniform effective normal stress, Equation 18 can be written in exactly the same form as Equation S22 of Skarbek et al. (2012), which in turn agrees with their numerical simulations with non-uniform slip within the VW segment (Skarbek et al. 2012, Figure 4). This agreement supports the adequacy of our simplifying assumption of uniform slip within the VW segment. Moreover, here we have derived the exact stability condition analytically rather than through the approximate approach of Skarbek et al. (2012).

Equation 18 is our basis to study the dependency of stability boundaries on various model parameters. The equation is too complicated to provide compact analytical expressions for the stability boundaries. We thus utilize a numerical method to solve it, and present the results in the next subsection. To verify this approach, in selected examples, we also solve Equation 10 numerically for λ and monitor its real part. Doing so, we confirm that both Equations 18 and 10 yield the same result, as expected. In section 4 we make further assumptions to develop approximate formulas for the stability boundaries.

3.3 LSA results

Similar to the QDYN simulations presented in section 2, for the LSA study we keep a_w, a_s, b_w, b_s, σ_s *and* D_{cs} fixed and vary the non-dimensional parameters α and β systematically. The LSA results are shown in Figure 3 along with our QDYN simulations results for two examples with $f = 1$ and $f = 1/7$. Despite the reduction of the problem to a two-degree-of-freedom system, the LSA results are in strikingly good agreement with the simulation results. This agreement builds confidence on the LSA and allows us to extend our study to a broader range of model parameters, because solving LSA is far more computational efficient than performing rate-and-state simulations. However, while LSA is a good predictor of fault stability, it provides more limited information about the instability. For instance, LSA does not predict whether an instability is seismic or aseismic, or whether or not slip is uniform across the VS and VW segments.

With the aid of LSA, we extend our study by varying the value of f (Figure 5), whereas we only examined three values in our QDYN simulations. We confirm that the asymptotic value of α along the T-instability boundary at large β (the horizontal branch of the T-boundary in Figure 5) is $\alpha_{Tc} \approx 1/f$.

We then relieve the constraint we placed on our previous rate-and-state simulations by fixing $\frac{\alpha}{\beta\xi^2}$. We now allow D_{cw} to vary freely and study the fault stability by varying α and $\xi^2 = D_{cw}/D_{cs}$ (Figure 9). Hereafter we refer to this parametric study as "the $\alpha - \xi$ system". The result is similar to varying α and β (hereafter referred to as "the $\alpha - \beta$ system"), except the horizontal axis is reversed, as larger D_{cw} in principle maps to smaller β when other parameters are fixed. The main observations are:

1. At large ξ, the fault is stable only if α is smaller than a certain value $\alpha_T(\xi)$. This corresponds to the T-instability previously investigated in the $\alpha - \beta$ system. The value of $\alpha_T(\xi)$ decreases with decreasing ξ. At large ξ, $\alpha_T(\xi) \propto \xi^2$. At intermediate ξ, $\alpha_T(\xi)$ converges to a near-constant value $\alpha_{Tc} \approx 1/f$, as was the case for the T-instability in the $\alpha - \beta$ system.

2. At ξ smaller than a certain value ξ_{min} (to the left of Figure 9), another stability boundary appears. This corresponds to the P-instability investigated in the $\alpha - \beta$ system. It converges with the T-instability boundary at ξ_{min}.

With the convenience of LSA we are able to study the effects of other non-dimensional numbers as well. The effect of L_{cs}/L is studied by varying the value of D_{cs}. An example of 10 times larger D_{cs} is shown in Figure 9. Doing so both the P-instability and T-instability boundaries are affected. The value of ξ^2_{min} decreases by a factor of 10, as expected, and the value of α_{Tc} increases. We also studied the effect of W' by varying the value of W. Figures 9, 10 and 11 show that the T-instability boundary is largely affected by changing W'. The β value along the vertical asymptotic limit of the T-instability boundary in the $\alpha - \beta$ system (Figures 11), β_{min}, is proportional to $1/W'$. The value of α along the horizontal asymptotic limit of the T-instability boundary (α_{Tc}), for both the $\alpha - \beta$ and $\alpha - \xi$ systems, is positively related to $1/W'$. The P-instability boundary does not change much with W'. This is expected as the P-instability boundary is mostly controlled by the self-stiffness of the VW segment, which is inversely proportional to its size L_w, and significantly larger than the fault bulk stiffness, which is inversely proportional to fault width W. The effects described above will be derived analytically in section 4.

4 Prediction of instability boundaries

In the previous section we have demonstrated that LSA accurately predicts the stability of the heterogeneous fault model. Yet the resulting equations are too complicated to make any straightforward predictions without solving the LSA equations numerically (Equations 10 or 18). In this section we will utilize suitable approximations to derive from Equation 18 compact formulas that accurately predict the instability boundaries.

4.1 T-instability boundary

4.1.1 Derivation of the T-instability boundary

We observed that slip is almost uniform near the T-instability boundary, i.e. the VW and VS segments of the fault have the same slip rate at any time: $V_w = V_s$. This observation allows us to approximate the connection between the VW and VS blocks as infinitely rigid, $K_{II} \to +\infty$. For convenience, we denote by $f_w = f/(1+f)$ and $f_s = 1/(1+f)$ the relative area occupied by the VW and VS segments, respectively. We also denote the spatial average of any physical property X as $\langle X \rangle = f_w X_w + f_s X_s$. Setting $K_{II} \to +\infty$ and defining $s_i' = s_i / K_{II}(1+f)$ we get:

$$s_0' = K_I \tag{19}$$

$$s_1' V_{pl} = \langle A - B \rangle + K_I (D_{cw} + D_{cs}) \tag{20}$$

$$s_2' V_{pl}^2 = (A D_c \rangle + (\langle (A-B)/D_c \rangle + K_I) D_{cw} D_{cs} \tag{21}$$

$$s_3' V_{pl}^3 = \langle A \rangle D_{cw} D_{cs} \tag{22}$$

$$s_4' = 0 \tag{23}$$

The condition at the instability boundary, Equation 18, is then reduced to:

$$s_1' s_2' = s_0' s_3' \tag{24}$$

This a quadratic equation for K_I:

$$K_I^2 + C_1 K_I + C_2 = 0 \tag{25}$$

where

$$C_1 = \langle A \rangle \left(\frac{1}{D_{cw}} + \frac{1}{D_{cs}} \right) - \left\langle \frac{B}{D_c} \right\rangle - \frac{\langle B \rangle}{D_{cw} + D_{cs}} \tag{26}$$

$$C_2 = \frac{\langle A - B \rangle}{D_{cw} + D_{cs}} \left(\langle A \rangle \left(\frac{1}{D_{cw}} + \frac{1}{D_{cs}} \right) - \left\langle \frac{B}{D_c} \right\rangle \right) \tag{27}$$

Equation 25 has two solutions:

$$K_I = \frac{1}{2} \left(-C_1 \pm C_1 \sqrt{1 - 4C_2/C_1^2} \right) \tag{28}$$

We determined in the homogeneous case and verified numerically in the heterogeneous case, that only the "+" solution is physical:

$$K_I = \frac{1}{2} \left(-C_1 + C_1 \sqrt{1 - 4C_2/C_1^2} \right) \tag{29}$$

Equation 29 is a closed form expression for the T-instability boundary. It is in perfect match with the complete LSA solution (Figure 10), except for a small difference at intermediate ξ in the unlikely case when the ratio between fault width and fault heterogeneity length scale W' is relatively small.

4.1.2 Asymptotic limits of the T-instability boundary

Based on Equation 29 we determine here the asymptotic behavior of the T-instability boundary.

a. Horizontal asymptotic limit. As discussed in sections 2 and 3.3 (Figure 5), in both the $\alpha - \beta$ and $\alpha - \xi$ systems, the T-instability boundary has a horizontal asymptote at large β and small ξ, respectively, of the form $\alpha \approx \alpha_{Tc} \approx 1/f$. Here we derive this asymptotic limit directly from Equation 29. The limits $\beta \to +\infty$ in the $\alpha - \beta$ system and $\xi \to 0$ in the $\alpha - \xi$ system correspond to $D_{cw} \to 0$. Setting that limit into Equation 29 we find that, asymptotically, the critical stiffness for T-instabilities on a mixed VW and VS fault is simply the spatial average of $(b - a)\sigma$ divided by the D_c value of the VS segment:

$$K_I = \frac{\langle B - A \rangle}{D_{cs}} \tag{30}$$

This equation can be written as

$$\frac{\pi G}{W} = \frac{f_s(b_s - a_s)\sigma_s + f_w(b_w - a_w)\sigma_w}{D_{cs}} \tag{31}$$

From this equation we derive the asymptotic critical α at the T-instability boundary:

$$\alpha_{Tc} = \frac{1}{f} + \frac{f+1}{f} \cdot \frac{\pi L_{cs}}{W} \tag{32}$$

In the usual case where $W \gg L_{cs}$, Equation 32 reduces to

$$\alpha_{Tc} \approx 1/f \tag{33}$$

b. Vertical asymptotic limit in the $\alpha - \beta$ system. We previously found that the fault is unstable for all values of α in the $\alpha - \beta$ system if $\beta < \beta_{min}$ and $\beta_{min} \propto 1/W'$ (Figures 11). This defines a vertical asymptotic instability boundary in the $\alpha - \beta$ system, with large α and fixed β, which implies $\sigma_w/\sigma_s \propto D_{cw}/D_{cs} \to +\infty$. Setting these two limits in Equation 29 gives

$$K_I = f_w(b_w - a_w)\sigma_w/D_{cw} \tag{34}$$

We can rewrite this equation as

$$\beta_{min} = L_w/L_{cw} = \pi/W' \tag{35}$$

4.1.3 Simplified approximation of the T-instability boundary

Here we further simplify Equation 29 thanks to a heuristic approximation. Numerical evaluation of the coefficients in Equation 29 shows that, for the range of parameters considered in our study, they satisfy $C_1^2 \gg C_2$. Second-order Taylor expansion of Equation 29 with respect to $4C_2/C_1^2$ gives $K_I \approx -C_2/C_1$. That is

$$K_I = \frac{\langle B - A \rangle}{D_{cw} + D_{cs}} \left(1 + \frac{\langle B \rangle}{D_{cw} + D_{cs}} \left(\langle A \rangle (1/D_{cw} + 1/D_{cs}) - \langle B/D_c \rangle - \langle B \rangle / (D_{cw} + D_{cs}) \right)^{-1} \right) \tag{36}$$

This is a very good approximation to the T-boundary in most of our simulations. However, in homogeneous media it is only valid if $B \approx A$. The asymptotic limits derived in section 4.1.2 also hold for the approximated Equation 36. Inspired by those asymptotic limits and the form of Equation 36, we propose an ultimately simplified equation for the T-instability boundary, which is in reasonably good approximation to the complete LSA results (Figure 9 and 10) and is also valid for homogeneous faults:

$$K_I = \frac{\langle B - A \rangle}{\max(D_{cw}, D_{cs})} \tag{37}$$

4.2 P-instability boundary

4.2.1 Derivation of the P-instability boundary

The interactions between VW and VS blocks cannot be ignored in attempts to predict the P-instability boundary. The stability limit $K_{II} = (B_w - A_w)/D_{cw}$ of an isolated VW block corresponds to a vertical P-instability boundary ($\beta = 1$) in the $\alpha - \beta$ system, which is inconsistent with the curved boundary found in our rate-and-state simulations and LSA results.

Here we derive an equation for the P-instability boundary from the complete LSA Equation 10. Because during P-instabilities only the VW block fails, the relevant stiffness is the stiffness K_{II} of the VW block, which is proportional

to the size of VW block ($L_w = f_w L$). The stiffness K_{II} is much larger than the stiffness K_I associated to uniform slip over the whole fault, which is proportional to the fault width, W. We thus simplify the coefficients in Equation 10 by setting $K_I = 0$ and get:

$$s_0 = 0 \tag{38}$$
$$s_1 = K_{II}(f(A_w - B_w) + (A_s - B_s))/V_{pl} \tag{39}$$
$$s_2 = ((A_w - B_w)(A_s - B_S) + K_{II}(f(A_w D_{cw} + (A_w - B_w)D_{cs}) + (A_s D_{cs} + (A_s - B_S)D_{cw})))/V_{pl}^2 \tag{40}$$
$$s_3 = (A_w A_s(D_{cw} + D_{cs}) - A_w B_s D_{cw} - A_s B_W D_{cs} + (A_s + fA_w)D_{cw}D_{cs}K_{II})/V_{pl}^3 \tag{41}$$
$$s_4 = A_w A_s D_{cw} D_{cs}/V_{pl}^4 \tag{42}$$

The condition at the instability boundary, Equation 18, becomes

$$s_1(s_4 s_1 - s_2 s_3) = 0 \tag{43}$$

Hence, either

$$s_1 = 0 \tag{44}$$

or

$$s_1 s_4 = s_2 s_3 \tag{45}$$

Equation 44 defines the velocity-neutral limit of the T-instability boundary in the limit $W \to +\infty$. Equation 45 properly defines the P-instability boundary. It yields a quadratic equation for K_{II}:

$$C_0 K_{II}^2 + C_1 K_{II} + C_2 = 0 \tag{46}$$

where

$$C_0 = (f(A_w D_{cw} + (A_w - B_w)D_{cs}) + (A_s D_{cs} + (A_s - B_s)D_{cw}))(A_s + fA_w)D_{cw}D_{cs} \tag{47}$$
$$\begin{aligned} C_1 = {} & (A_w - B_w)(A_s - B_s)(A_s + fA_w)D_{cw}D_{cs} + (f(A_s D_{cw} + (A_w - B_w)D_{cs}) \\ & + (A_s D_{cs} + (A_s - B_s)D_{cw}))(A_w D_{cw}(A_s - B_s) + A_s D_{cs}(A_w - B_w)) \\ & - (f(A_w - B_w) + (A_s - B_s))A_w A_s D_{cw} D_{cs} \end{aligned} \tag{48}$$
$$C_2 = (A_w - B_w)(A_s - B_s)(A_w D_{cw}(A_s - B_S) + A_s D_{cs}(A_w - B_w)) \tag{49}$$

Equation 46 has two solutions:

$$K_{II} = \frac{-C_1}{2C_0}\left(1 \pm \sqrt{1 - \frac{4C_0 C_2}{C_1^2}}\right) \tag{50}$$

Numerical examination shows the physical solution is the one with "+" sign:

$$K_{II} = \frac{-C_1}{2C_0}\left(1 + \sqrt{1 - \frac{4C_0 C_2}{C_1^2}}\right) \tag{51}$$

Equation 51 accurately defines the P-instability boundary in closed form. It is in perfect match with the complete LSA solution for the range of parameters we have considered (thus we only plotted the LSA results in our figures).

4.2.2 Simplified approximation of the P-instability boundary

Similar to how we approximated the T-instability boundary in section 4.1.3, we manipulate Equation 51 to further simplify the P-instability boundary equation. Numerical evaluation shows that, within the range of parameters considered in our study, heterogeneous faults satisfy $C_1^2 >> C_0 C_2$. First-order Taylor expansion of Equation 51 with respect to $4C_1^2/(C_0 C_2)$ gives $K_{II} \approx -C_1/C_0$. That is

$$\begin{aligned} K_{II} \approx {} & \frac{A_w(B_s - A_s)/D_{cs} + A_s(B_w - A_w)/D_{cw}}{A_s + fA_w} \\ & - \frac{(A_w - B_w)(A_s - B_s)(A_s + fA_w) - (f(A_w - B_w) + (A_s - B_s))A_w A_s}{(f(A_w D_{cw} + (A_w - B_w)D_{cs})/D_{cw}D_{cs} + (A_s D_{cs} + (A_s - B_s)D_{cw}))(A_s + fA_w)} \end{aligned} \tag{52}$$

Numerical inspection shows that the first term in Equation 52 is much larger than the second term. We thus approximate and further simplify the P-instability boundary equation by ignoring the second term:

$$K_{II} \approx \frac{A_w(B_s - A_s)/D_{cs} + A_s(B_w - A_w)/D_{cw}}{A_s + fA_w} \tag{53}$$

This approximation of the P-instability boundary matches surprisingly well the complete LSA results for all parameter settings we have explored (Figures 9 and 10).

Equation 53 is in a form simple enough that we can examine the P-instability boundary directly. When $D_{cw} \ll D_{cs}$, Equation 53 reduces to

$$K_{II} \approx \frac{B_w - A_w}{D_{cw}} \frac{A_s}{A_s + fA_w} \tag{54}$$

The first term in Equation 54 is exactly the critical stiffness of an isolated VW block, while the second term approximates the effect of the interaction with the VS block. The latter term shows why the P-boundary is not vertical in the $\alpha - \beta$ system.

5 Discussion and conclusions

We have presented a systematic numerical and theoretical study of the stability of slip on faults with a regular alternation of frictional properties and effective normal stress. Our results paint a comprehensive picture of how the stability of a heterogeneous fault is affected by the relative proportion of strong and weak materials, and by their relative strength and other frictional properties. These results help us gain insight on natural slip processes over a wide range of spatial-temporal scales and have implications for earthquake hazard estimation. In particular, a fault composed in its majority of material with stable properties can actually be unstable, and a stable fault can become unstable due to time-dependent changes of strength contrast.

In this study, we assumed uniform slip within the VW segment, treating it as a single cell in our QDYN simulations. This assumption allows us to conduct the computational study of fault instabilities more efficiently. The stability transitions in simulations that do resolve the non-uniform slip distribution inside each asperity (Figure 4 of Skarbek et al. (2012)) may be broader than in our simulations. However, both in our work and in that of Skarbek et al. (2012) the position of the stability boundaries is well predicted by linear stability analysis. Thus the assumption of uniform slip within the VW segment is an adequate approximation for the scope of our study: it does not affect the position of stability boundaries, only their width in the model parameter space. We note that a wider transition from steady slip to episodic fast slip as a function of asperity size occurs in simulations under the aging law than under the slip law, when the ratio a/b is high (Figure 5 of Rubin (2008)). The transition under the aging law occurs at asperity sizes between two nucleation length scales L_c and L_∞, defined in Rubin and Ampuero (2005), and is broader at higher a/b because $L_c/L_\infty \sim 1/(1 - a/b)$. However, the L_∞ length is irrelevant under the slip law (Ampuero and Rubin 2008), which is the state evolution law adopted here because it is more consistent with laboratory experiments with large velocity jumps, large enough to model the propagating front of slip transients (Bhattacharya et al. 2015). Simulation results presented by Luo (2018) indicate that the width of the transition is more fundamentally affected by the range of scales of heterogeneity than by the choice of state evolution law.

The proportion of strong and weak materials in a fault zone is controlled by structural and geometrical properties such as the distribution of asperity sizes and the spacing between asperities. These properties may evolve through mechanical processes like asperity fragmentation and dispersion driven by fault zone shearing, and physico-chemical processes like alteration assisted by fault zone fluids. These processes typically operate on time scales much longer than an earthquake cycle and on length scales comparable to the seismogenic width. An evolution of asperities controlled by the irreversible process of fragmentation and shearing would lead to monotonically decreasing asperity sizes and increasing asperity spacing as a function of depth. This would be inconsistent with the fact that seismic slip events within otherwise aseismic slip areas. (e.g. Obara and Kato 2016; Yamashita et al. 2015) Furthermore, it is not a viable candidate mechanism for depth-dependent slip behavior on strike-slip faults.

In contrast, the relative strength between asperities and matrix may change over short spatial-temporal scales and non-monotonically with depth. Depth-dependent changes of temperature and effective normal stress are obvious factors that can affect the strong and weak materials differently. Another plausible factor, which can further introduce heterogeneity along-strike and over shorter scales, are changes of the fluid pressure difference between matrix and asperities in a fault zone with hydraulically sealed asperities. Pressure in the permeable matrix can increase with depth

due to dehydration, without affecting the pressure inside hydraulically sealed asperities. On the other hand, laboratory experiments of VW/VS compound materials (e.g. Saffer and Marone 2003) show that natural illite shale exhibits only VS behavior and no strong velocity-dependent friction over a large range of normal stress and loading velocity. Thus the smectite-illite transition alone does not support the seismic-aseismic transition in subduction zones, and an additional mechanism is required. Nevertheless, smectite-to-illite transitions release chemically bound fluid and can cause an increase in pore pressure. Thus our model of depth-dependent asperity/matrix fluid pressure contrast is a mechanism to consider.

In cases when differential pore pressure is already present, a uniform change in normal stress or pore pressure can cause a large change in the asperity/matrix strength contrast. Possible scenarios of temporal relative strength change include: transient surface or tidal loadings that affects normal stress; slow pressure build-up in the matrix; fluid injection; sudden decrease of fluid pressure in asperities due to seal breaking. The fault-valve mechanism during earthquakes changes the local permeability of fault materials and ultimately results in fluctuation of pore pressure over times scale of earthquake cycles. In particular, since the depths at which slow slip and tremor occur have been inferred to have very high pore pressure (thus low effective normal stress), a small uniform change of pore pressure (i.e. some amount comparable to effective normal stress and much smaller than the total pore pressure or normal stress) can lead to a large fluctuation in asperity/matrix relative strength. In addition, if the change of relative strength destabilizes the slow slip zone it could facilitate the nucleation of regular earthquakes (Figure 3).

We found that a monotonic increase of pore pressure can lead a fault with micro-seismic activity produced by T-instabilities to a large rupture with an intermediate period of stable slip (Figure 3 at intermediate β). This is reminiscent of the natural phenomenon of seismic quiescence, i.e. a period of greatly reduced seismicity observed before certain large earthquakes (Habermann 1988; Kanamori 1981; Sobolev 2011).

The model presented here is a promising framework to understand the full spectrum of slow-to-fast earthquakes. Figure 12 shows conceptually the transitions of fault behavior of a subduction fault as a function of depth (orange curve in the left figure). Near the surface the relative strength between VW and VS segments is low, so the fault is stable. The relative strength increases with increasing depth and the fault transits into unstable and slow events like shallow SSE, LFE and tremors. The relative strength keeps increasing at seismogenic depth and the fault transits from slow earthquakes to fast earthquakes, including regular earthquakes of various magnitudes and megathrust earthquakes rupturing the whole seismogenic zone. Then the relative strength starts to decrease and the fault behavior transits back to slow earthquakes again, producing deep episodic tremor and SSE. The relative strength continues decreasing with depth and the fault eventually transit into stable steady slip. Alternatively, if the individual criticalness of the VW asperity increases, due for instance to a decrease of D_c or an increase of effective normal stress, it may enter the regime of background tremor activity in which individual VW asperities fail spontaneously, as indicated by the dotted orange curve in Figure 12.

Our study serves as a building block for models of episodic tremor and slow-slip that emphasize the role of fault heterogeneity. In particular, results reported here on the conditions required for T-instabilities provided guidance on how to set the asperity/matrix relative strength in the models of slow slip and tremor developed by Luo (2018). Such models quantitatively reproduced observations of slow slip and tremor migration patterns in Cascadia and revealed a new mechanism of slow slip driven by tremors. While the minimalistic model studied in the present work involves a single heterogeneity length scale (L), natural faults are heterogeneous across a broad range of length scales (e.g. Fagereng 2011). The range of slow to fast slip transition may increase significantly when such diversity of heterogeneity scales are considered (Luo 2018).

A Appendices

A.1 Derivation of governing equations

In this section we derive the stress balance governing equations of a two-degree-of-freedom spring block system with alternating VW and VS segments as depicted in Figure 8. We first derive it starting from the discrete version of the stress balance equations, implying an integer ratio $1/f$ between VS and VW areas. We then extend it to arbitrary f.

The VW and VS materials in our QDYN simulations are arranged in a periodical pattern, with one VW block (index $i = 0$) and m VS blocks (indices $i = 1, ..., m$). We define the slip deficit of the i-th block as:

$$\delta_i = V_{pl}t - d_i \tag{A.1}$$

where V_{pl} is the plate velocity and d_i is the slip of the i-th block. Under the quasi-static approximation, the shear stress of each block is determined by the slip deficit of every block in the system through a linear relation:

$$\tau_i = K_{ij}\delta_j \tag{A.2}$$

where K_{ij} is the shear stress in the i-th block induced by a unitary slip deficit on the j-th block. With periodic boundary conditions, the static stress transfer matrix K has the following properties:

$$K_{ij} = K_{|i-j|} \qquad \text{symmetric Toeplitz structure} \tag{A.3}$$

$$\sum_{i=0}^{m} K_i = K_w \doteq \pi G/W \qquad \text{stiffness of uniform slip} \tag{A.4}$$

$$K_i = K_{m+1-i} \qquad \text{periodicity, i.e. } K_1 = K_m, K_2 = K_{m-1}\ldots \tag{A.5}$$

Combining Equations A.1 and A.2, using the symmetry of the kernel (Equation A.3) gives:

$$\tau_0 = K_0\delta_0 + K_1\delta_1 + K_2\delta_2 + \ldots + K_3\delta_{m-2} + K_2\delta_{m-1} + K_1\delta_m \tag{A.6}$$

$$\tau_1 = K_1\delta_0 + K_0\delta_1 + K_1\delta_2 + \ldots + K_4\delta_{m-2} + K_3\delta_{m-1} + K_2\delta_m \tag{A.7}$$

$$\tau_2 = K_2\delta_0 + K_1\delta_1 + K_0\delta_2 + \ldots + K_5\delta_{m-2} + K_4\delta_{m-1} + K_3\delta_m \tag{A.8}$$

$$\ldots$$

$$\tau_{m-1} = K_2\delta_0 + K_3\delta_1 + K_4\delta_2 + \ldots + K_1\delta_{m-2} + K_0\delta_{m-1} + K_1\delta_m \tag{A.9}$$

$$\tau_m = K_1\delta_0 + K_2\delta_1 + K_3\delta_2 + \ldots + K_2\delta_{m-2} + K_1\delta_{m-1} + K_0\delta_m \tag{A.10}$$

If we assume uniform slip d_s in the VS part:

$$\delta_1 = \delta_2 = \ldots = \delta_m = V_{pl}t - d_s \doteq \delta_s \tag{A.11}$$

then the stress in the VW segment is

$$\tau_w = \tau_0 = K_0\delta_w + (K_w - K_0)\delta_s \tag{A.12}$$

We rearrange this equation as

$$\tau_w = K_w\delta_w + (K_w - K_0)(\delta_s - \delta_w) \tag{A.13}$$

We define the average stress τ_s in the VS region as

$$\tau_s = (\tau_1 + \tau_2 + \tau_3 + \ldots + \tau_m)/m \tag{A.14}$$

Adding up the shear stresses and using Equation A.4, we get

$$\sum_{i=0}^{m}\tau_i = \sum_{i=0}^{m}\sum_{j=0}^{m} K_{ij}\delta_j = \sum_{j=0}^{m}\left(\sum_{i=0}^{m} K_{ij}\right)\delta_j = K_w\sum_{i=0}^{m}\delta_i \tag{A.15}$$

That is

$$\tau_w + m\tau_s = K_w(\delta_w + m\delta_s) \tag{A.16}$$

Combining Equations A.16 and A.13 we get:

$$\tau_s = K_w\delta_s + (K_w - K_0)/m \cdot (\delta_w - \delta_s) \tag{A.17}$$

Equations A.13 and A.17 define the stress balance governing equations in discrete media. The derivation is so far restricted to integer values of the VS to VW area ratio, $1/f = m$. We make the assumption that the result can be extended to arbitrary values of f, in particular to non-integer $1/f$ values. The resulting governing equations are

$$\tau_w = K_I(V_{pl}t - d_w) + K_{II}(d_s - d_w) \tag{A.18}$$

$$\tau_s = K_I(V_{pl}t - d_s) + fK_{II}(d_w - d_s) \tag{A.19}$$

where $K_I = K_w = \pi G/W$ is the loading stiffness, $K_{II} = K_0 - K_w$ the stiffness of block interactions, and K_0 the self-stiffness of the VW block. The latter can be derived from the stress transfer kernel for a 1D fault with period L

embedded in 2D homogeneous media, discretized by $N = L/\Delta x$ cell of uniform size Δx (Ampuero 2002, Appendix 2C):

$$K_{ij} = \frac{\pi G}{L} \frac{\sin(\pi/N)}{\sin(\frac{|i-j|-1/2}{N})\ \sin(\frac{|i-j|+1/2}{N})} \tag{A.20}$$

Taking $i = j$, we get the self-stiffness of the VW block:

$$K_0 = \frac{2\pi G}{L} \frac{\sin(\pi/N)}{\cos(\frac{1}{N}) - 1} \tag{A.21}$$

A.2 Approximate account for fault width via a 2.5D approximation

Here we derive the static stress kernel for the 2.5D approximation introduced in section 3.1. Because our model has periodic boundary conditions and the QDYN code employs the Fast Fourier Transform for efficiency, we consider here the Fourier transform $\tilde{K}$ of the kernel. In an infinite fault in 3D it is given by Equation 20 of Andrews (1981). Here instead, by analogy to the expression in 2D (Ampuero et al. 2002),

$$\tilde{K}(k) = \frac{G}{2}\,|k| \tag{A.22}$$

where k is the spatial wave number, we consider the following 3D proxy

$$\tilde{K}(k_x, k_z) = \frac{G}{2}\,\sqrt{k_x^2 + k_z^2} \tag{A.23}$$

where k_x and k_z are wavenumbers in the along-strike and along-dip directions, respectively. This expression is exact only for the case where Poisson's ratio is zero, which is not typical in rocks, but it is mathematically convenient and shares the essential properties of the exact kernel. In the 2.5D approximation we assume that the depth-distribution of slip is fixed, the same at all positions along strike, and equal to a sinusoidal function of wavelength equal to the width of the slip area, W. This implies $k_z = 2\pi/W$ and Equation (A.22) becomes:

$$\tilde{K}(k_x) = \frac{G}{2}\,\sqrt{k_x^2 + (2\pi/W)^2} \tag{A.24}$$

This is the spectral domain kernel adopted in our QDYN simulations for periodic faults.

A.3 Linear stability analysis of a two-degree-of-freedom periodic spring-block system

Here we derive the matrix Q involved in the linear stability analysis of a two-degree-of-freedom periodic spring-block system under rate-and-state friction. We denote $F(V, \theta)$ the friction coefficient and $E(V, \theta)$ the state evolution law. The subscript $i = w$ or s indicates the VW or the VS block, respectively. The rate-and-state friction equations are

$$\tau_i = \sigma_i F(\theta_i, v_i) = \sigma_i F_i \tag{A.25}$$

$$\dot{\theta}_i = E(\theta_i, v_i) = E_i \tag{A.26}$$

Small perturbation (marked with *) near a reference steady state yields:

$$\tau_i^* = \sigma_i (F_{iv} v_i^* + F_{i\theta} \theta_i^*) \tag{A.27}$$

$$\dot{\theta}_i^* = E_{iv} v_i^* + E_{i\theta} \theta_i^* \tag{A.28}$$

where subscripts v and θ denote the partial derivative with respect to that variable, evaluated at the reference steady state. We re-write Equation (A.27) as

$$\theta_i^* = (\tau_i^*/\sigma_i - F_{iv} v_i^*)/F_{i\theta} \tag{A.29}$$

Taking the time derivative of Equation (A.29) and combining that with Equation (A.28) yields

$$\dot{\tau_i^*} = \sigma_i F_{iv} \dot{v_i^*} + \sigma_i F_{i\theta} (E_{iv} v_i^* + E_{i\theta} \theta_i^*) \tag{A.30}$$

Substituting θ_i^* in Equation (A.30) with Equation (A.29) gives

$$\dot{\tau_i^*} = \sigma_i F_{iv} \dot{v_i^*} + \sigma_i (F_{i\theta} E_{iv} - F_{iv} E_{i\theta}) v_i^* + E_{i\theta} \tau_i^* \tag{A.31}$$

Taking the time derivative of Equation (A.31) yields

$$\ddot{\tau_i^*} = \sigma_i F_{iv} \ddot{v_i^*} + \sigma_i (F_{i\theta} E_{iv} - F_{iv} E_{i\theta}) \dot{v_i^*} + E_{i\theta} \dot{\tau_i^*} \tag{A.32}$$

Taking the time derivative and small perturbation near steady-state of Equation (A.18) gives

$$\dot{\tau_w^*} = -K_I \dot{v_w^*} + K_{II} (\dot{v_s^*} - \dot{v_w^*}) \tag{A.33}$$

Taking the time derivative again:

$$\ddot{\tau_w^*} = -K_I \ddot{v_w^*} + K_{II} (\ddot{v_s^*} - \ddot{v_w^*}) \tag{A.34}$$

Considering the VW block, $i = w$, and substituting $\dot{\tau_w^*}$ and $\ddot{\tau_w^*}$ in Equation (A.32) with Equations (A.33) and (A.34) gives

$$\sigma_w F_{wv} \ddot{v_w^*} + (\sigma_w F_{w\theta} E_{wv} - \sigma_w F_{wv} E_{w\theta} + K_I + K_{II}) \dot{v_w^*} - K_{II} \dot{v_s^*} - (K_I + K_{II}) E_{w\theta} v_w^* + K_{II} E_{w\theta} v_s^* = 0 \tag{A.35}$$

Similarly for the VS block, $i = s$,

$$\dot{\tau_s^*} = -K_I \dot{v_s^*} + f K_{II} (\dot{v_w^*} - \dot{v_s^*}) \tag{A.36}$$

$$\ddot{\tau_s^*} = -K_I \ddot{v_s^*} + f K_{II} (\ddot{v_w^*} - \ddot{v_s^*}) \tag{A.37}$$

$$\sigma_s F_{sv} \ddot{v_s^*} + (\sigma_s F_{s\theta} E_{sv} - \sigma_s F_{sv} E_{s\theta} + K_I + f K_{II}) \dot{v_s^*} - f K_{II} \dot{v_w^*} - (K_I + f K_{II}) E_{s\theta} v_s^* + f K_{II} E_{s\theta} v_w^* = 0 \tag{A.38}$$

Equations (A.35) and (A.38) form a system of second order coupled ODEs with general form

$$\bar{\bar{M}}_2 \ddot{\vec{v}} + \bar{\bar{M}}_1 \dot{\vec{v}} + \bar{\bar{M}}_0 \vec{v} = \vec{0} \tag{A.39}$$

We seek solutions of the form

$$\vec{v} = \vec{v}(0) e^{\lambda t} \tag{A.40}$$

Then Equation (A.39) becomes

$$\begin{aligned} Q(\lambda) = & \begin{pmatrix} F_{wv}\sigma_w & 0 \\ 0 & F_{sv}\sigma_s \end{pmatrix} \lambda^2 \\ & + \begin{pmatrix} \sigma_w F_{w\theta} E_{wv} - \sigma_w F_{wv} E_{w\theta} + K_I + K_{II} & -K_{II} \\ -f K_{II} & \sigma_s F_{s\theta} E_{sv} - \sigma_s F_{sv} E_{s\theta} + K_I + f K_{II} \end{pmatrix} \lambda \\ & + \begin{pmatrix} -(K_I + K_{II}) E_{w\theta} v_w^* & K_{II} E_{w\theta} \\ f K_{II} E_{s\theta} & -(K_I + f K_{II}) E_{s\theta} \end{pmatrix} \end{aligned} \tag{A.41}$$

For rate-and-state friction the partial derivatives evaluated at steady state are:

$$F_{iv} = \frac{a_i}{V_{pl}} \tag{A.42}$$

$$F_{i\theta} = \frac{b_i V_{pl}}{D_{ci}} \tag{A.43}$$

$$E_{iv} = -\frac{1}{V_{pl}} \tag{A.44}$$

$$E_{i\theta} = -\frac{V_{pl}}{D_{ci}} \tag{A.45}$$

Finally, we get

$$\begin{aligned} Q(\lambda) = & \begin{pmatrix} a_w\sigma_w/V_{pl} & 0 \\ 0 & a_s\sigma_s/V_{pl} \end{pmatrix} \lambda^2 \\ & + \begin{pmatrix} (a_w - b_w)\sigma_w/D_{cw} + K_I + K_{II} & -K_{II} \\ -f K_{II} & (a_s - b_s)\sigma_s/D_{cs} + K_I + f K_{II} \end{pmatrix} \lambda \\ & + \begin{pmatrix} (K_I + K_{II}) V_{pl}/D_{cw} & -K_{II} V_{pl}/D_{cw} \\ -f K_{II} V_{pl}/D_{cs} & (K_I + f K_{II}) V_{pl}/D_{cs} \end{pmatrix} \end{aligned} \tag{A.46}$$

Acknowledgements

We acknowledge support from the National Science Foundation awards EAR-1015698 and EAR-1151926 and from the Southern California Earthquake Center (Contribution No. 7946). SCEC is funded by NSF Cooperative Agreement EAR-1033462 and USGS Cooperative Agreement G12AC20038.

References

Ampuero, J. P. (2002), "Etude physique et numérique de la nucléation des séismes". *PhD Thesis, University of Paris VII, France*.

Ampuero, J. P. and A. M. Rubin (2008), "Earthquake nucleation on rate and state faults–Aging and slip laws". *Journal of Geophysical Research: Solid Earth*, 113 (B1). B01302.

Ampuero, J. P., J. P. Vilotte, and F. J. Sanchez-Sesma (2002), "Nucleation of rupture under slip dependent friction law: simple models of fault zone". *Journal of Geophysical Research: Solid Earth*, 107 (B12). 2324.

Ando, R., R. Nakata, and T. Hori (2010), "A slip pulse model with fault heterogeneity for low-frequency earthquakes and tremor along plate interfaces". *Geophysical Research Letters*, 37 (10).

Andrews, D. J. (1981), "A stochastic fault model: 2. Time-dependent case". *Journal of Geophysical Research: Solid Earth*, 86 (B11), pp. 10821–10834.

Avouac, J. P., L. Meng, S. Wei, T. Wang, and J. P. Ampuero (2015), "Lower edge of locked Main Himalayan Thrust unzipped by the 2015 Gorkha earthquake". *Nature Geoscience*, 8 (9), pp. 708–711.

Bebout, G. E. and M. D. Barton (2002), "Tectonic and metasomatic mixing in a high-T, subduction-zone mélange—insights into the geochemical evolution of the slab–mantle interface". *Chemical Geology*, 187 (1), pp. 79–106.

Bhattacharya, P., A. M. Rubin, E. Bayart, H. M. Savage, and C. Marone (2015), "Critical evaluation of state evolution laws in rate and state friction: Fitting large velocity steps in simulated fault gouge with time-, slip-, and stress-dependent constitutive laws". *Journal of Geophysical Research: Solid Earth*, 120 (9), pp. 6365–6385.

Burridge, R. and L. Knopoff (1967), "Model and theoretical seismicity". *Bulletin of the seismological society of america*, 57 (3), pp. 341–371.

Chen, T. and N. Lapusta (2009), "Scaling of small repeating earthquakes explained by interaction of seismic and aseismic slip in a rate and state fault model". *Journal of Geophysical Research: Solid Earth*, 114 (B1). B01311.

Dieterich, J. H. (1979), "Modeling of rock friction: 1. Experimental results and constitutive equations". *Journal of Geophysical Research: Solid Earth*, 84 (B5), pp. 2161–2168.

Dragert, H. (2007), "Mediating plate convergence". *Science*, 315 (5811), pp. 471–472.

Dublanchet, P., P. Bernard, and P. Favreau (2013), "Interactions and triggering in a 3-D rate-and-state asperity model". *Journal of Geophysical Research: Solid Earth*, 118 (5), pp. 2225–2245.

Fagereng, Å. (2011), "Fractal vein distributions within a fault-fracture mesh in an exhumed accretionary mélange, Chrystalls Beach Complex, New Zealand". *Journal of Structural Geology*, 33 (5), pp. 918–927.

Fagereng, Å. and A. F. Cooper (2010), "The metamorphic history of rocks buried, accreted and exhumed in an accretionary prism: an example from the Otago Schist, New Zealand". *Journal of Metamorphic Geology*, 28 (9), pp. 935–954.

Fagereng, Å. and R. Sibson (2010), "Melange rheology and seismic style". *Geology*, 38 (8), pp. 751–754.

Fagereng, Å. and S. A. den Hartog (2017), "Subduction megathrust creep governed by pressure solution and frictional-viscous flow". *Nature Geoscience*, 10 (1), pp. 51–57.

Glendinning, P. (1994), *Stability, instability and chaos: an introduction to the theory of nonlinear differential equations*. Vol. 11. Cambridge university press.

Gomberg, J. et al. (2010), "Slow-slip phenomena in Cascadia from 2007 and beyond: A review". *Geological Society of America Bulletin*, 122 (7-8), pp. 963–978.

Gu, Y. and T. Wong (1994), "Nonlinear Dynamics of the Transition from Stable Sliding to Cyclic Stick-Slip in Rock". *Nonlinear Dynamics and Predictability of Geophysical Phenomena*, pp. 15–35.

Habermann, R. E. (1988), "Precursory seismic quiescence: past, present, and future". *Pure and applied Geophysics*, 126 (2), pp. 279–318.

Hawthorne, J. C. and A. M. Rubin (2013), "Laterally propagating slow slip events in a rate and state friction model with a velocity-weakening to velocity-strengthening transition". *Journal of Geophysical Research: Solid Earth*, 118 (7), pp. 3785–3808.

Healy, J. H., W. W. Rubey, D. T. Griggs, and C. B. Raleigh (1968), "The denver earthquakes". *Science*, 161 (3848), pp. 1301–1310.

Hillers, G. and S. A. Miller (2007), "Dilatancy controlled spatiotemporal slip evolution of a sealed fault with spatial variations of the pore pressure". *Geophysical Journal International*, 168 (1), pp. 431–445.

Hillers, G., Y. Ben-Zion, and P. M. Mai (2006), "Seismicity on a fault controlled by rate-and state-dependent friction with spatial variations of the critical slip distance". *Journal of Geophysical Research: Solid Earth*, 111 (B1). B01403.

Hillers, G., P. M. Mai, Y. Ben-Zion, and J. P. Ampuero (2007), "Statistical properties of seismicity of fault zones at different evolutionary stages". *Geophysical Journal International*, 169 (2), pp. 515–533.

Hyndman, R. D. and K. Wang (1993), "Thermal constraints on the zone of major thrust earthquake failure: The Cascadia subduction zone". *Journal of Geophysical Research: Solid Earth*, 98 (B2), pp. 2039–2060.

Ide, S., G. C. Beroza, D. R. Shelly, and T. Uchide (2007), "A scaling law for slow earthquakes". *Nature*, 447 (7140), p. 76.

Ito, Y., K. Obara, K. Shiomi, S. Sekine, and H. Hirose (2007), "Slow earthquakes coincident with episodic tremors and slow slip events". *Science*, 315 (5811), pp. 503–506.

Kanamori, H. (1981), "The nature of seismicity patterns before large earthquakes". *Earthquake Prediction*, pp. 1–19.

Kocharyan, G. G., V. A. Novikov, A. A. Ostapchuk, and D. V. Pavlov (2016), "A study of different fault slip modes governed by the gouge material composition in laboratory experiments". *Geophysical Journal International*, ggw409.

Lay, T. and H. Kanamori (1981), "An asperity model of large earthquake sequences". *Earthquake prediction*, pp. 579–592.

Lay, T., H. Kanamori, C. J. Ammon, K. D Koper, A. R. Hutko, L. Ye, H. Yue, and T. M. Rushing (2012), "Depth-varying rupture properties of subduction zone megathrust faults". *Journal of Geophysical Research: Solid Earth*, 117 (B4). B04311.

Leeman, JR, DM Saffer, MM Scuderi, and C Marone (2016), "Laboratory observations of slow earthquakes and the spectrum of tectonic fault slip modes". *Nature communications*, 7. 11104.

Luo, X. and G. Vasseur (2002), "Natural hydraulic cracking: numerical model and sensitivity study". *Earth and Planetary Science Letters*, 201 (2), pp. 431–446.

Luo, Y. (2018), "Earthquake Moment-Area Scaling Relations and the Effect of Fault Heterogeneity on Slow to Fast Earthquake Slip". PhD thesis. California Institute of Technology.

Luo, Y., J. P. Ampuero, P. Galvez, M. Ende, and B. Idini (2017a), *QDYN: a Quasi-DYNamic earthquake simulator (v1.1)*. DOI: 10.5281/zenodo.322459. URL: https://doi.org/10.5281/zenodo.322459.

Luo, Y., J. P. Ampuero, K. Miyakoshi, and K. Irikura (2017b), "Surface Rupture Effects on Earthquake Moment-Area Scaling Relations". *Pure and Applied Geophysics*, pp. 1–12.

Ma, S. and C. He (2001), "Period doubling as a result of slip complexities in sliding surfaces with strength heterogeneity". *Tectonophysics*, 337 (1), pp. 135–145.

Marone, C. (1998), "Laboratory-derived friction laws and their application to seismic faulting". *Annual Review of Earth and Planetary Sciences*, 26 (1), pp. 643–696.

Marone, C. and B. Kilgore (1993), "Scaling of the critical slip distance for seismic faulting with shear strain in fault zones". *Nature*, 362 (6421), pp. 618–621.

Mclaskey, G. C. and F. Yamashita (2017), "Slow and fast ruptures on a laboratory fault controlled by loading characteristics". *Journal of Geophysical Research: Solid Earth*, pp. 3719–3738.

Meneghini, F., G. Di Toro, C. D. Rowe, J. C. Moore, A. Tsutsumi, and A. Yamaguchi (2010), "Record of mega-earthquakes in subduction thrusts: the black fault rocks of Pasagshak Point (Kodiak Island, Alaska)". *Geological Society of America Bulletin*, 122 (7-8), pp. 1280–1297.

Meng, L., A. Inbal, and J. P. Ampuero (2011), "A window into the complexity of the dynamic rupture of the 2011 Mw 9 Tohoku-Oki earthquake". *Geophysical Research Letters*, 38 (7). L00G07.

Nakata, R., R. Ando, T. Hori, and S. Ide (2011), "Generation mechanism of slow earthquakes: Numerical analysis based on a dynamic model with brittle-ductile mixed fault heterogeneity". *Journal of Geophysical Research: Solid Earth*, 116 (B8). B08308.

Obara, K. and A. Kato (2016), "Connecting slow earthquakes to huge earthquakes". *Science*, 353 (6296), pp. 253–257.

Osborne, M. J. and R. E. Swarbrick (1997), "Mechanisms for generating overpressure in sedimentary basins: a reevaluation". *AAPG bulletin*, 81 (6), pp. 1023–1041.

Parsons, T. (2005), "A hypothesis for delayed dynamic earthquake triggering". *Geophysical Research Letters*, 32 (4). L04302.

Peacock, S. M. (2009), "Thermal and metamorphic environment of subduction zone episodic tremor and slip". *Journal of Geophysical Research: Solid Earth*, 114 (B8).

Perfettini, H. and J. P. Ampuero (2008), "Dynamics of a velocity strengthening fault region: Implications for slow earthquakes and postseismic slip". *Journal of Geophysical Research: Solid Earth*, 113 (B9). B09411.

Perfettini, H., M. Campillo, and I. Ionescu (2003), "On the scaling of the slip weakening rate of heterogeneous faults". *Journal of Geophysical Research: Solid Earth*, 108 (B9). 2410.

Rice, J. R. (1993), "Spatio-temporal complexity of slip on a fault". *Journal of Geophysical Research: Solid Earth*, 98 (B6), pp. 9885–9907.

Rice, J. R. and Y. Ben-Zion (1996), "Slip complexity in earthquake fault models". *Proceedings of the National Academy of Sciences*, 93 (9), pp. 3811–3818.

Rittenhouse, G. (1971), "Mechanical compaction of sands containing different percentages of ductile grains: a theoretical approach". *Bulletin - American Association of Petroleum Geologists*, 55 (1), pp. 92–96.

Roberts, S. J. and J. A. Nunn (1995), "Episodic fluid expulsion from geopressured sediments". *Marine and Petroleum Geology*, 12 (2), 195IN1203–202IN3204.

Rogers, G. and H. Dragert (2003), "Episodic tremor and slip on the Cascadia subduction zone: The chatter of silent slip". *Science*, 300 (5627), pp. 1942–1943.

Rubin, A. M. (2008), "Episodic slow slip events and rate-and-state friction". *Journal of Geophysical Research: Solid Earth*, 113 (B11). B11414.

Rubin, A. M. and J. P. Ampuero (2005), "Earthquake nucleation on (aging) rate and state faults". *Journal of Geophysical Research: Solid Earth*, 110 (B11). B11312.

Ruina, A. (1983), "Slip instability and state variable friction laws". *Journal of Geophysical Research: Solid Earth*, 88 (B12), pp. 10359–10370.

Saffer, D. M. and C. Marone (2003), "Comparison of smectite-and illite-rich gouge frictional properties: application to the updip limit of the seismogenic zone along subduction megathrusts". *Earth and Planetary Science Letters*, 215 (1), pp. 219–235.

Scuderi, M. M. and C. Collettini (2016), "The role of fluid pressure in induced vs. triggered seismicity: Insights from rock deformation experiments on carbonates". *Scientific reports*, 6, p. 24852.

Seno, T. (2003), "Fractal asperities, invasion of barriers, and interplate earthquakes". *Earth, planets and space*, 55 (11), pp. 649–665.

Sibson, R. (1992), "Implications of fault-valve behaviour for rupture nucleation and recurrence". *Tectonophysics*, 211 (1-4), pp. 283–293.

— (2014), "Earthquake rupturing in fluid-overpressured crust: how common?" *Pure and Applied Geophysics*, 171 (11), pp. 2867–2885.

Sibson, R., F. Robert, and K. H. Poulsen (1988), "High-angle reverse faults, fluid-pressure cycling, and mesothermal gold-quartz deposits". *Geology*, 16 (6), pp. 551–555.

Skarbek, R. M., A. W. Rempel, and D. A. Schmidt (2012), "Geologic heterogeneity can produce aseismic slip transients". *Geophysical Research Letters*, 39 (21). L21306.

Sobolev, G. (2011), "Seismic Quiescence and Activation". *Encyclopedia of Solid Earth Geophysics*. Springer, pp. 1178–1184.

Tse, S. T. and J. R. Rice (1986), "Crustal earthquake instability in relation to the depth variation of frictional slip properties". *Journal of Geophysical Research: Solid Earth*, 91 (B9), pp. 9452–9472.

Venkataraman, A. and H. Kanamori (2004), "Observational constraints on the fracture energy of subduction zone earthquakes". *Journal of Geophysical Research: Solid Earth*, 109 (B5). B05302.

Viesca, R. C. (2016), "Stable and unstable development of an interfacial sliding instability". *Physical Review E*, 93 (6), p. 060202.

Wech, A. G. and K. C. Creager (2011), "A continuum of stress, strength and slip in the Cascadia subduction zone". *Nature Geoscience*, 4 (9), p. 624.

Yabe, S. and S. Ide (2017), "Slip-behavior transitions of a heterogeneous linear fault". *Journal of Geophysical Research: Solid Earth*, 122 (1), pp. 387–410.

Yamashita, Y. et al. (2015), "Migrating tremor off southern Kyushu as evidence for slow slip of a shallow subduction interface". *Science*, 348 (6235), pp. 676–679.

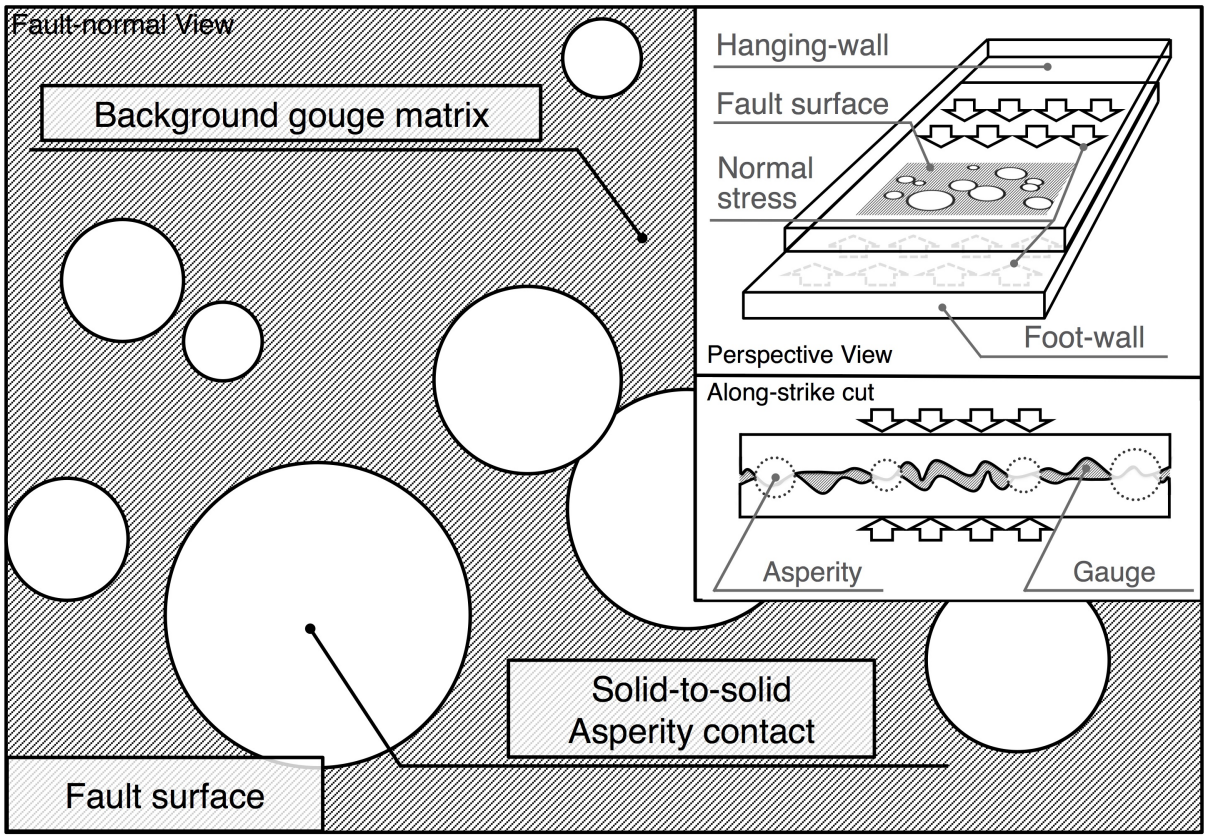

Figure 1: Sketch of conceptual model. Two rough surfaces make contact at discrete asperities. Fault gouge is sandwiched between the surfaces and surrounds the asperities. The gouge matrix which can have different compressibility and permeability than the asperities.

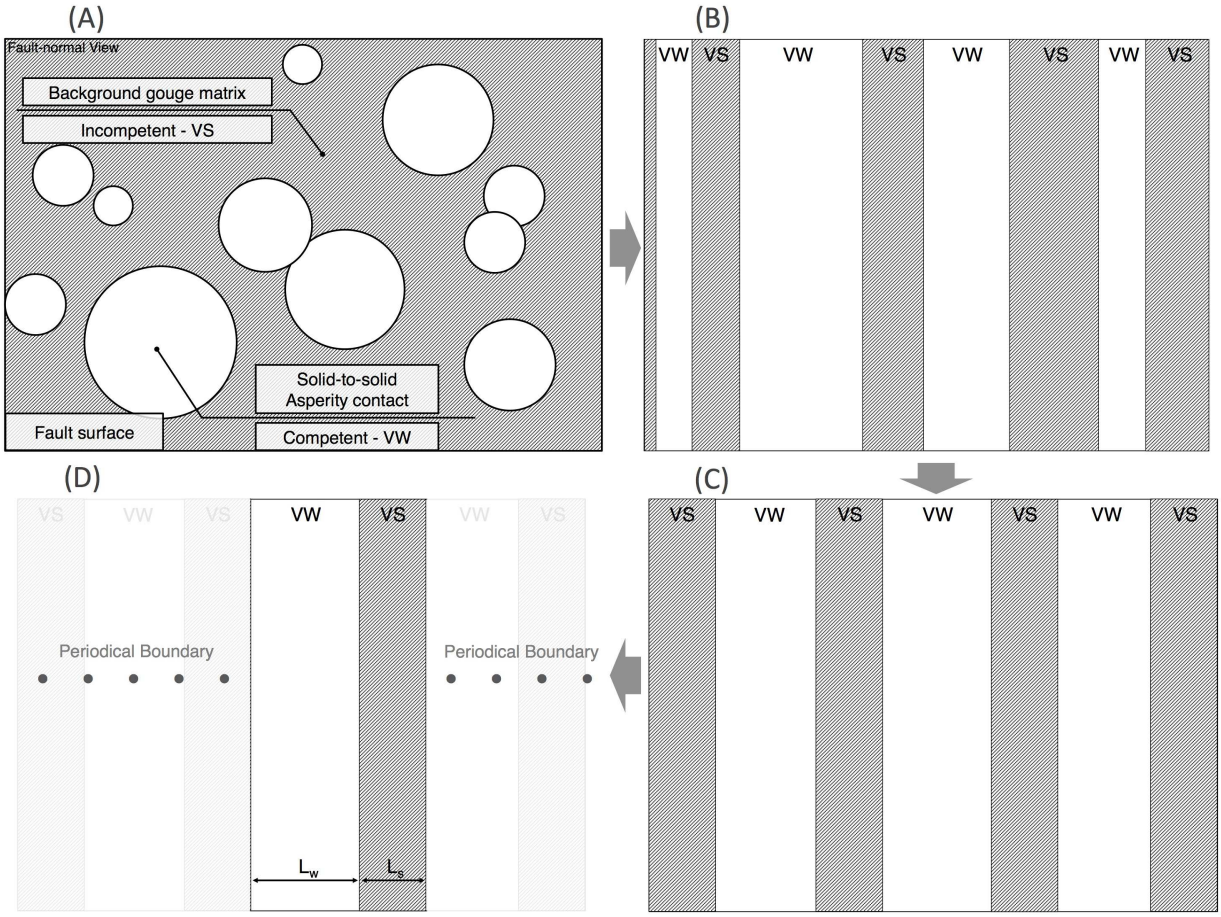

Figure 2: Realization and simplification of the conceptual model. (A) The asperities and the gouge matrix are represented as VW and VS materials, respectively. (B) They are both simplified as along-dip strips. (C) The strips are assumed to be regularly distributed in space. (D) The pattern of VW and VS materials is assumed to be periodic along-strike (with length of L_w and L_s, respectively). The fault is reduced to a infinitely long, linear fault in a 2D medium with periodic alternation of VW and VS segments.

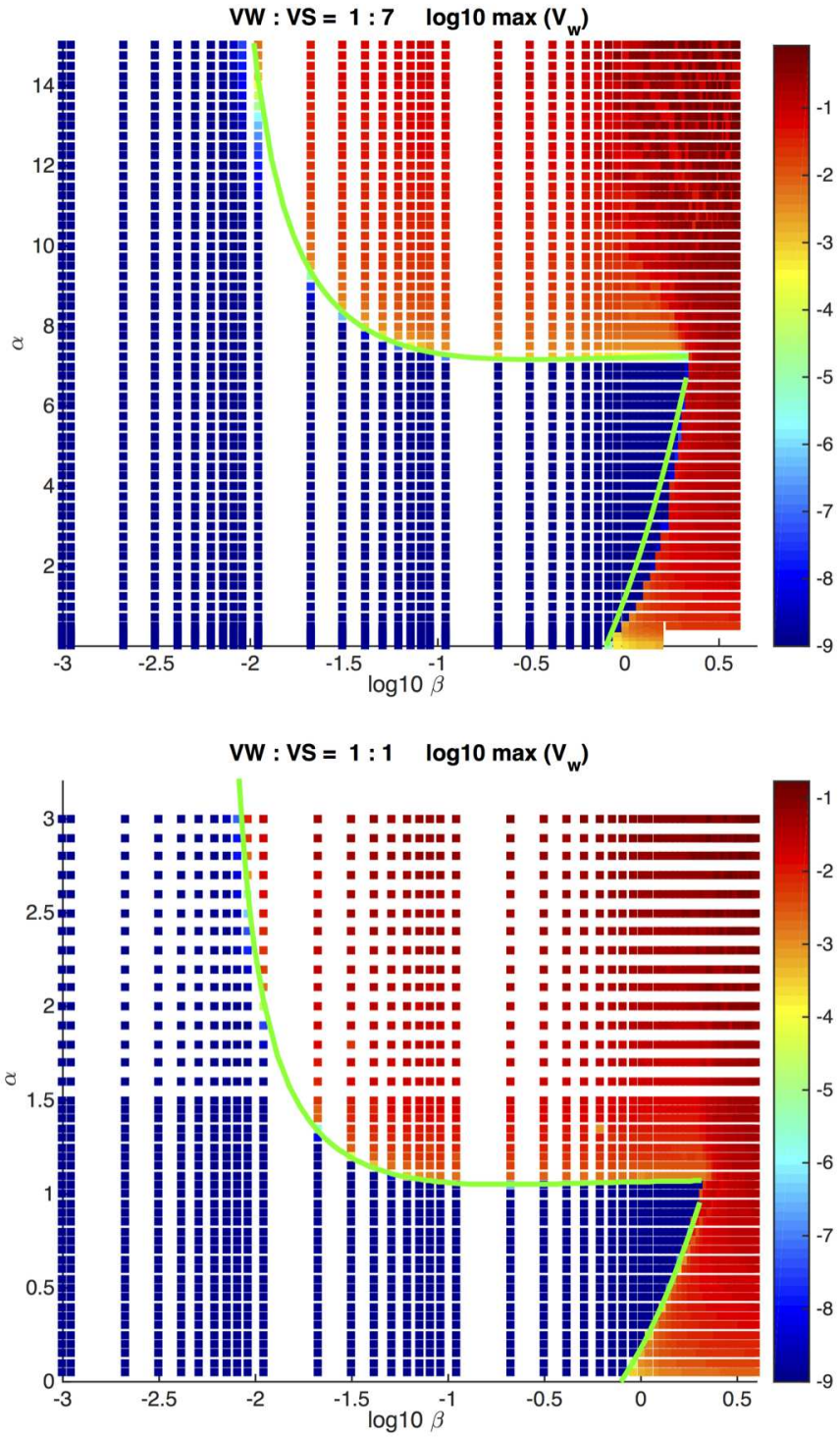

Figure 3: Stability of a heterogeneous VW/VS fault as a function of relative strength α and criticalness of the VW segment β, for VW/VS area ratios $f = 1/7$ (top) and $f = 1$ (bottom). Results of both QDYN simulations and linear stability analysis (LSA) are shown. Colored squares indicate the logarithm of peak slip rate (see color bar) reached in the VW segment in QDYN simulations, after the "warm-up" cycles. Each square is obtained from a separate simulation. Green solid curves are the stability boundaries determined by LSA.

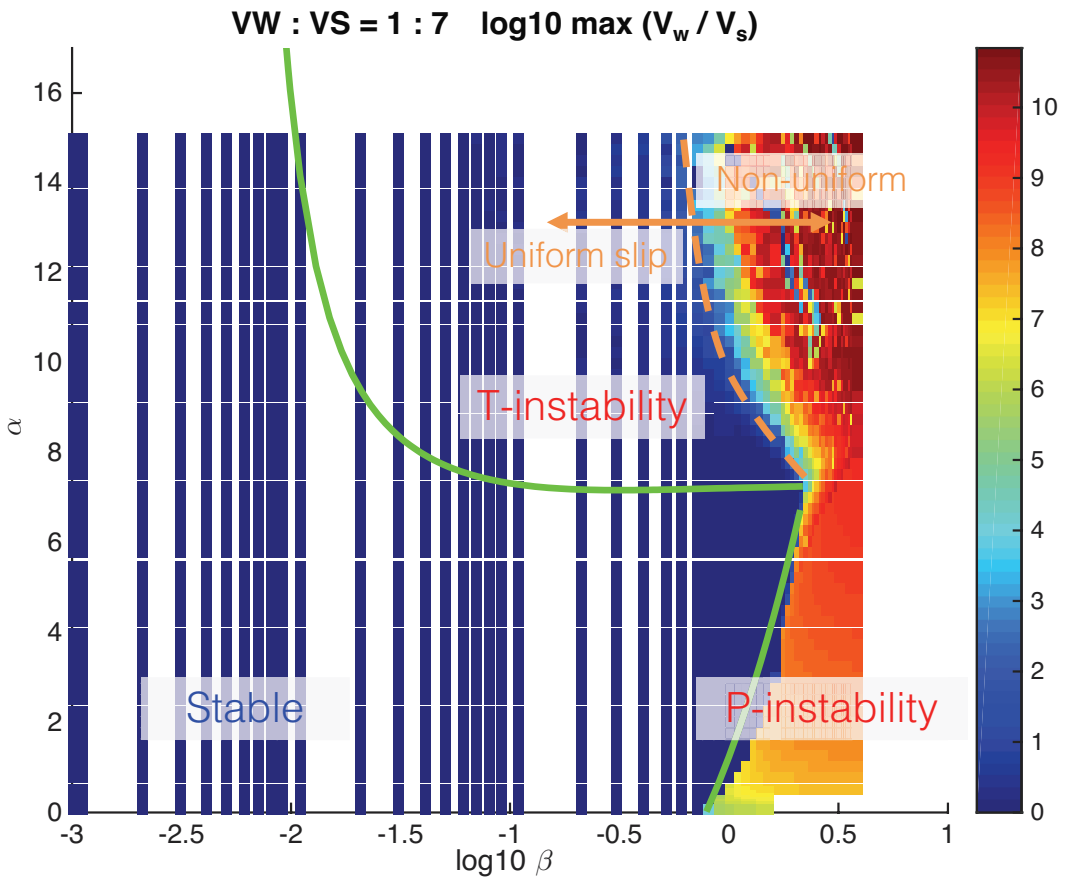

Figure 4: Analogous to Figure 1, but colors now indicate the maximum slip rate contrast between the VW segment and the center of VS segment (maximum ratio of slip rate measured at the VW segment and in the center of VS segment at the same time). A large slip rate contrast in general means slip is non-uniform over the fault. Green solid curve: LSA results (Equation 10). Orange dash curve: approximate boundary of T-instability with uniform and non-uniform slip.

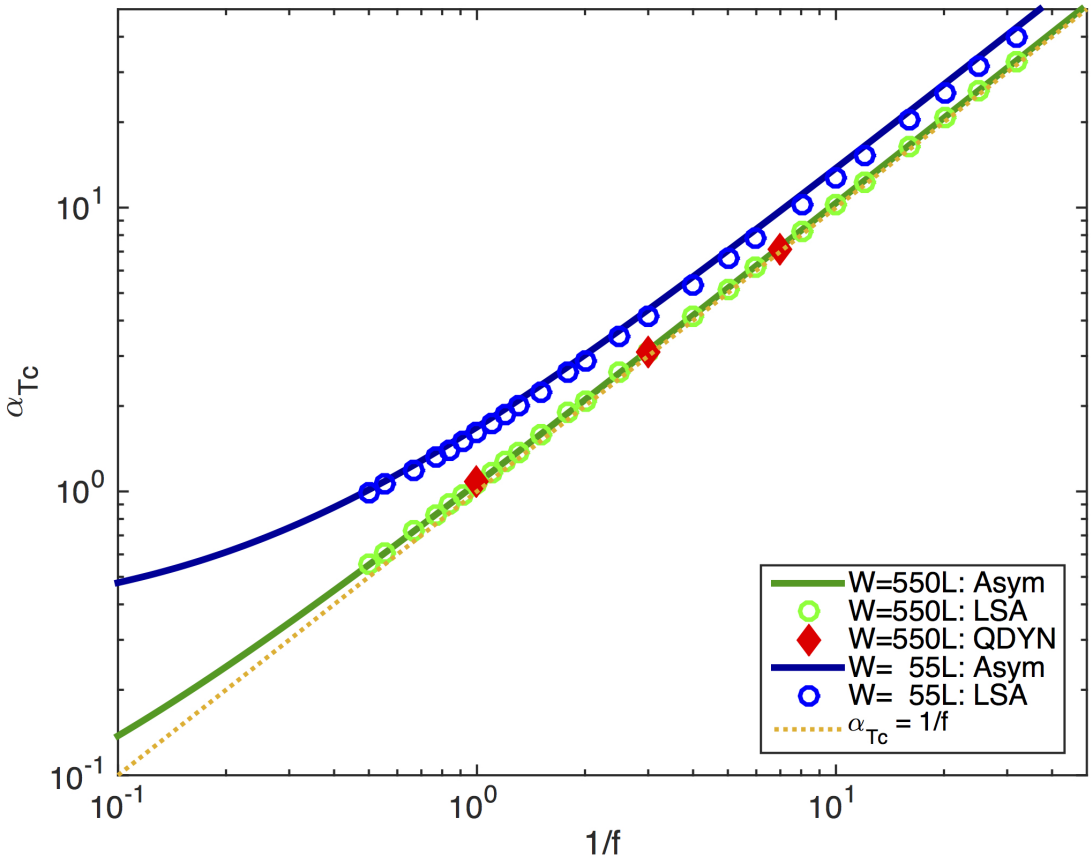

Figure 5: Comparison of the horizontal asymptotic limit α_{Tc} between QDYN simulations, LSA, and simplified equations with various f values. Red diamonds: α_{Tc} measured from QDYN simulations, with $f = 1$, $1/3$ and $1/7$, and $W = 550L$. Green circles: α_{Tc} measured from full LSA results (Equation 10), $W = 550L$. Dark green solid curve: asymptotic Equation 32 with $W = 550L$. Golden dotted line: $\alpha_{Tc} = 1/f$. Blue circles and solid curve: α_{Tc} measured from full LSA (Equation 10) and asymptotic Equation 32 with $W = 55L$.

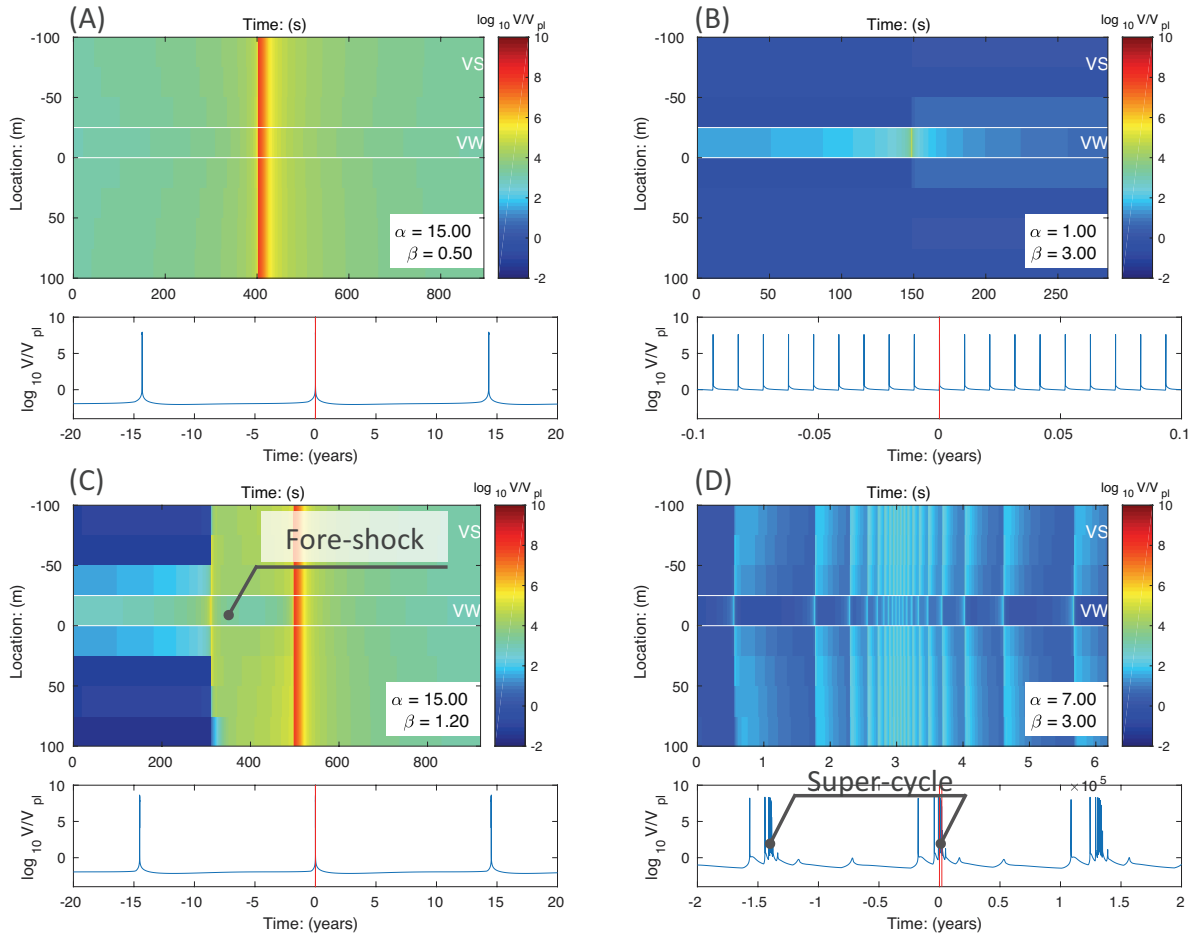

Figure 6: Slip patterns in simulations with different VW self-criticalness β and relative strength contrast α. Each subplot is one representative simulation with $f = 1/7$. The lower panel shows the logarithm of the maximum slip rate normalized by loading rate V_{pl} as a function of time (years). The upper panel shows the logarithm of slip rate normalized by loading rate V_{pl} as a function of time (seconds) and location, zoomed in within the time window indicated by red bars in the lower panel. The boundary of the VW segment is indicated by white lines. Note the different time scales in each example. (A) Typical T-instability, the whole fault ruptures with inter-event time in the order of years (controlled by fault width W). (B) Typical P-instability, rupture is mainly confined to the VW segment, with inter-event time in the order of days (controlled by VW segment size L_w). (C) T-instability with fore-shock(s), in which a large event that ruptures the whole fault is preceded by smaller event(s) rupturing part of the fault. (D) "Hybrid" behavior in which T-instability super-cycles with long recurrence times are interspersed by clustered occurrences of P-instabilities with short intervals.

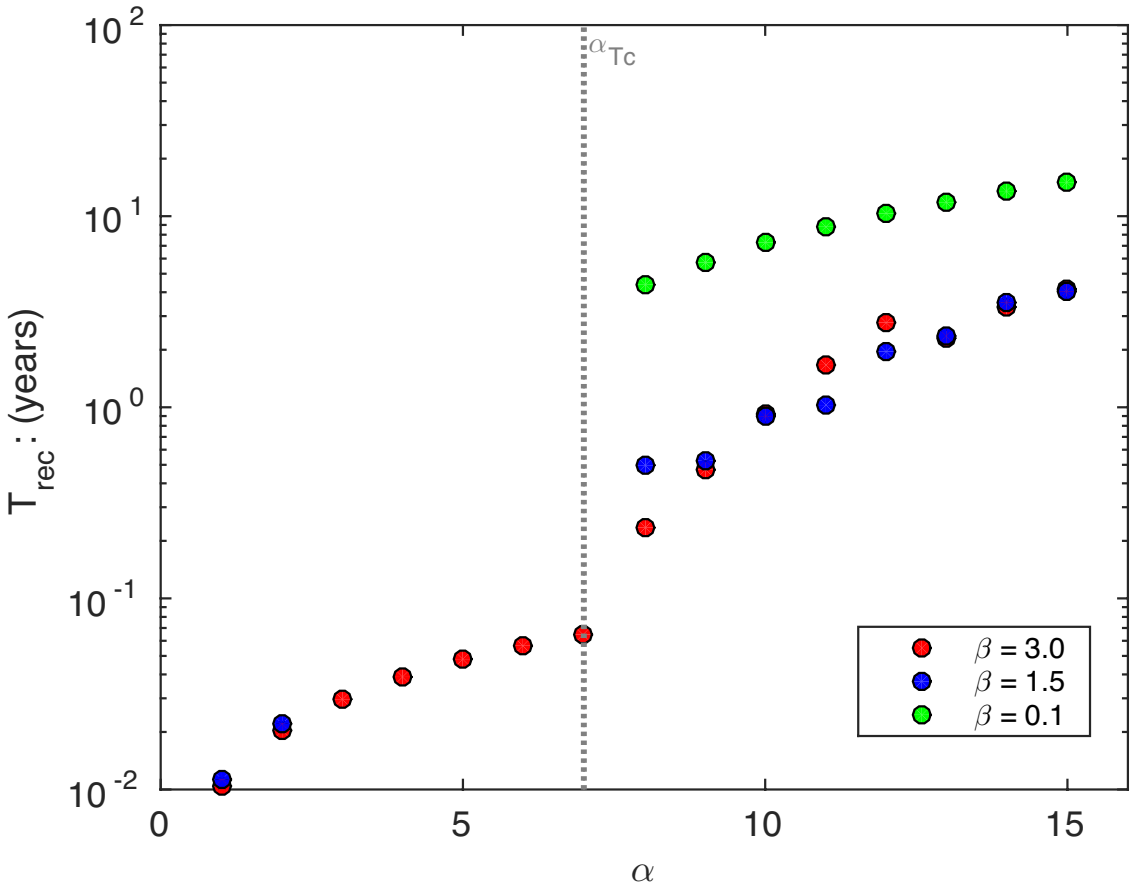

Figure 7: Measured average inter-event time of models with different VW self-criticalness β as a function of relative strength α. Grey dotted line: $\alpha_{Tc} = 1/f$, which in general separates T-instability and P-instability. The inter-event times increase with increasing α. When the relative strength is above α_{Tc} the inter-event time is in the order of years, whereas below α_{Tc} the inter-event time is in the order of days.

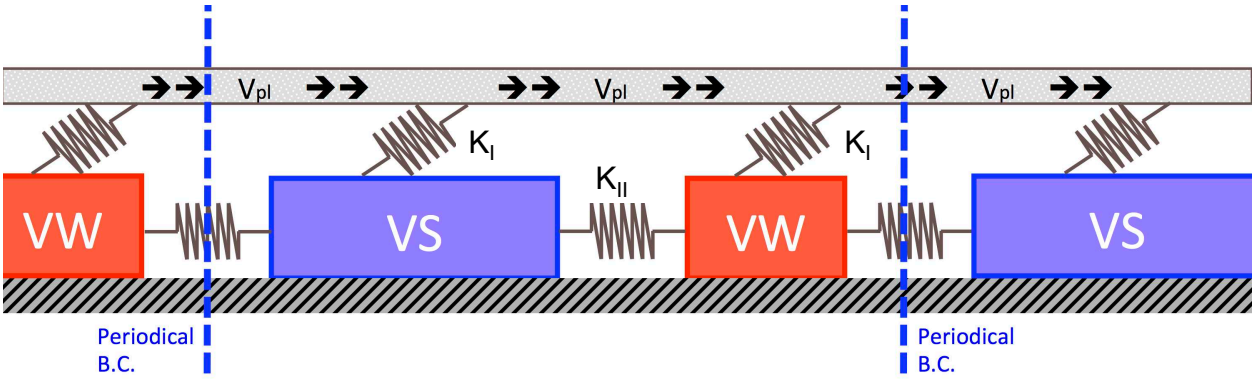

Figure 8: Periodic two-degree-of-freedom spring-block system. The system consists of a periodical arrangement of two VW and VS blocks inter-connected by a spring, and both loaded with side springs at constant speed.

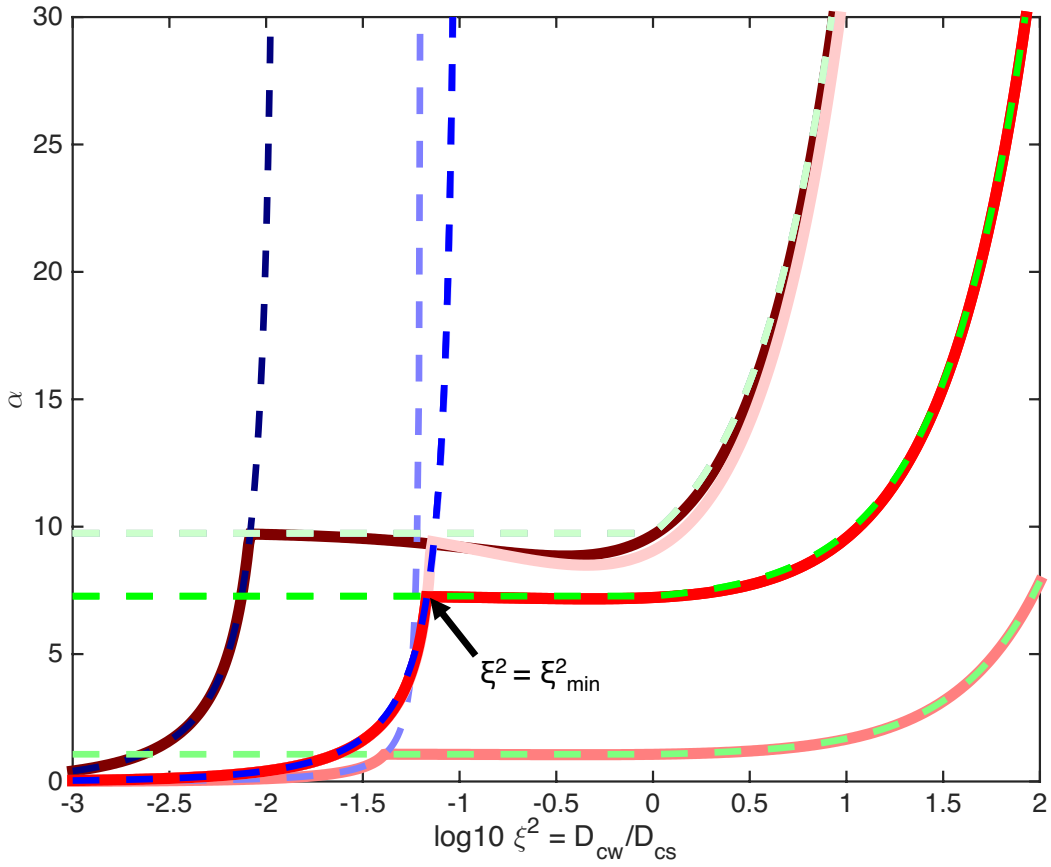

Figure 9: Instability boundary with respect to α and ξ. Red solid curve: full LSA results (Equation 10) with parameter settings of table 1, $D_{cs} = 4 \times 10^{-4}$ m. Blue dashed curve: approximation Equation 53 for the P-instability boundary. Green dashed curve: approximation Equation 37 for the T-instability boundary. Lighter colors represent cases with $f = 1$. Darker colors (leftmost maroon solid curve with corresponding dashed curves) represent cases with $f = 1/7$ and 10 times larger D_{cs} (4×10^{-3} m). Lightest colors represent cases with $f = 1/7$ and 10 times smaller W' ($W' = 55$). The T-instability boundary is identical to the case with $W' = 550$ per Equation 37. Black arrow shows one example of T-instability boundary (right) converging with the P-instability boundary (left) at $\xi = \xi_{min}$. The values of all other parameters not mentioned here are those in table 1.

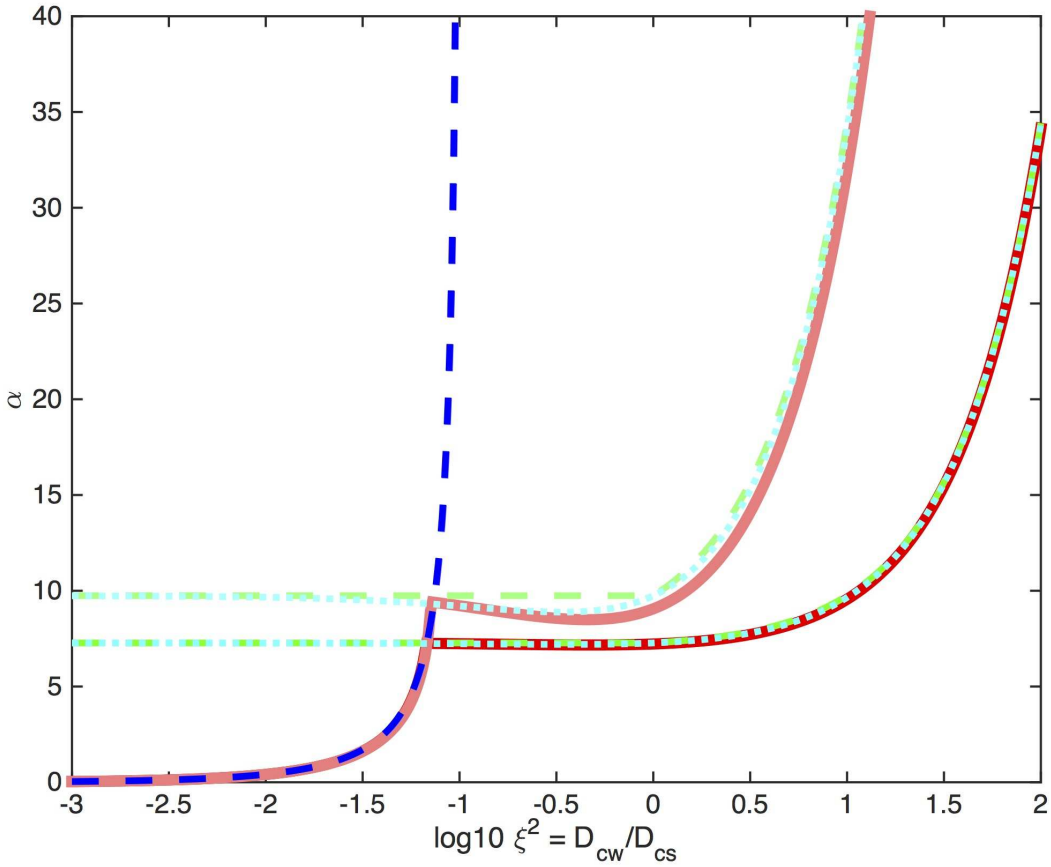

Figure 10: Analogous to Figure 9. Instability boundary with respect to α and ξ, with $f = 1/7$. Red solid curve: full LSA results (Equation 10), same as in Figure 9. Blue dashed curve: approximation Equation 53 for the P-instability boundary. Aqua dotted curve: approximation Equation 29 for the T-instability boundary. Green dashed curve: approximation Equation 37 for the T-instability boundary. Lighter colors represent cases with 10 times smaller W' ($W' = 55$).

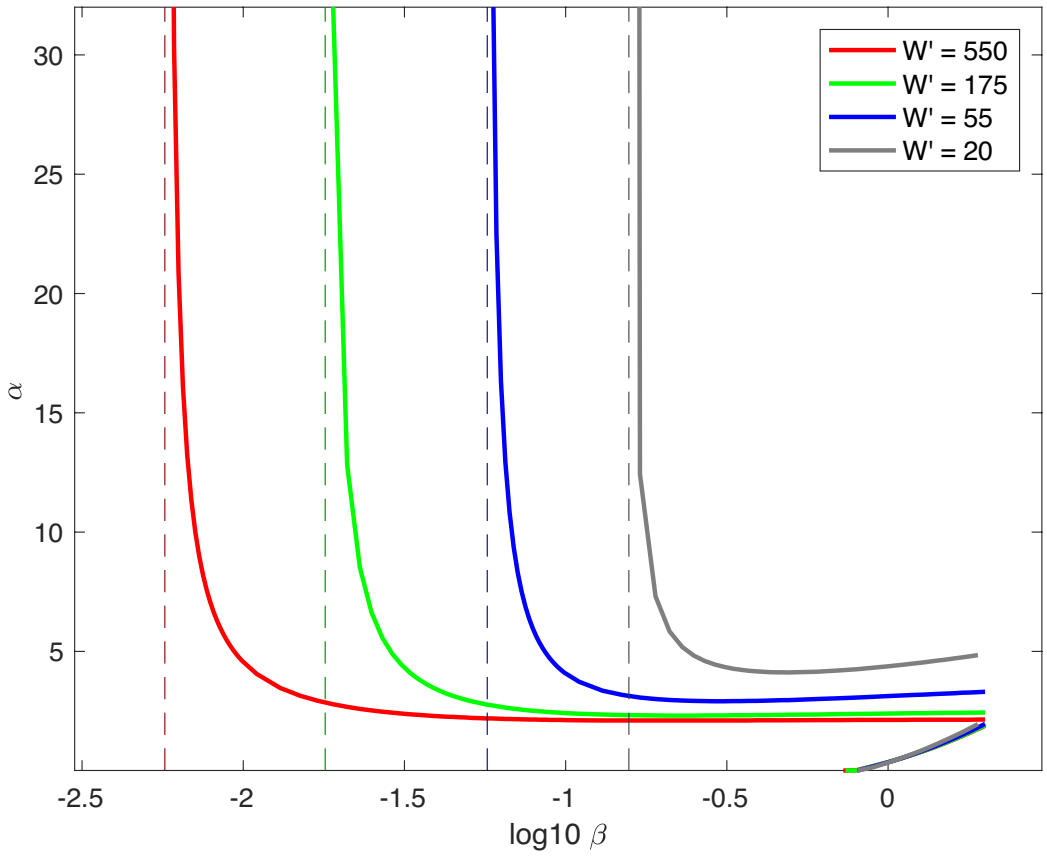

Figure 11: Instability boundary in the $\alpha - \beta$ system for various values of W'. Solid curve: LSA results. Vertical dashed lines with corresponding color: vertical asymptotic limit of $\beta_{min} = \pi/W'$ (Equation 35).

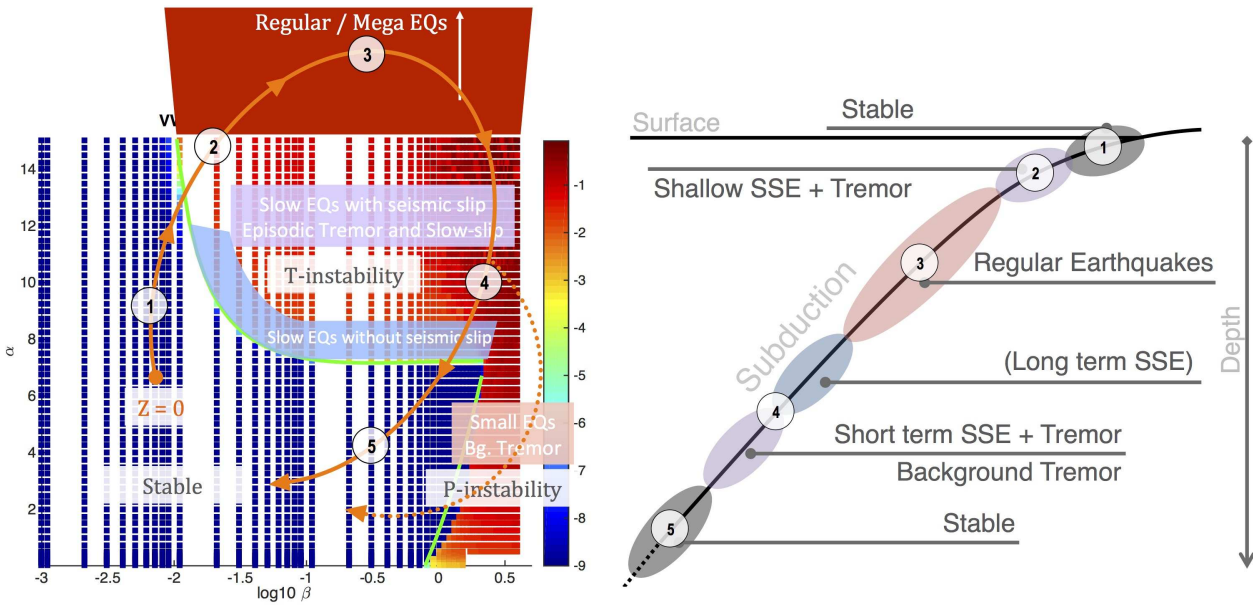

Figure 12: Conceptual interpretation of the transition between fast and slow earthquakes in a subduction zone in the framework of our model results.